

Direct measurement of the $\bar{K}N \rightarrow \pi\Sigma$ scattering amplitude below the $\bar{K}N$ threshold employing the $d(K^-, N)\pi\Sigma^-$ reaction

Kentaro Inoue

January 6, 2020

Contents

| | |
|---|----------|
| 1 Data analysis | 3 |
| 1.1 Over view | 3 |
| 1.2 Beam line | 4 |
| 1.2.1 T0 and BHD aanalysis | 4 |
| 1.2.2 Beam line chamer | 4 |
| 1.2.3 Beam momentum analyzer - D5 magnet | 6 |
| 1.2.4 BLC2-BPC matching | 7 |
| 1.2.5 Irradiated kaon number | 8 |
| 1.3 CDS | 9 |
| 1.3.1 CDC tracking | 9 |
| 1.3.2 CDH | 10 |
| 1.3.3 Vertex reconstruction | 11 |
| 1.3.4 Particle identification | 12 |
| 1.3.5 Time walk correcction of CDC | 12 |
| 1.3.6 Recunstruced hyperons by CDS | 14 |
| 1.3.7 CDC efficeicny | 14 |
| 1.4 Forward counter | 14 |
| 1.4.1 Forward proton analysis | 15 |
| 1.4.2 Time offset turning | 18 |
| 1.4.3 Consistency check using invariant mass of $\Lambda\pi^-$ by the CDS | 18 |
| 1.4.4 $d(K^-, p)\pi^-\Lambda$ and $d(K^-, p)\pi^-\Sigma^0$ identification | 20 |
| 1.4.5 Conversion factor of the $d(K^-, p)$ | 22 |
| 1.4.6 $d(K^-, p)\pi^-Sigma^0$ and $d(K^-, p)\pi^-\Lambda$ cross section | 23 |
| 1.4.7 Neutron counter | 24 |
| 1.4.8 NC efficiency estimation | 27 |
| 1.4.9 Neutron overkill by the BVC/CVC | 30 |
| 1.4.10 High order correction for dE | 30 |
| 1.4.11 $d(K^-, n)$ scaling factor | 31 |
| 1.4.12 $K^-d \rightarrow n\pi^+\pi^-n$ reactions | 31 |
| 1.4.13 template fitting of $d(K^-, n\pi^+\pi^-)n$ final state | 33 |
| 1.4.14 The cross section of K^0 | 37 |
| 1.4.15 The cross section of the $d(K^-, n)\pi^\mp\Sigma^\pm$ | 41 |

Chapter 1

Data analysis

1.1 Over view

In this chapter, beam line is explained first of all. Slow extraction beam had RF structure and secondary beam has particles pass abnormal trajectory. Beam line analysis aim at rejection of beam that is not kaon and define kaon beam. Beam line analysis evaluates number of irradiated kaon.

Next, CDS is explained. CDC performed tracking of decayed particles in the Sorenoid magnet and decided reaction vertex with BPC. CDH measured timing of decayed particle and identified these with momentum reconstructed by CDC.

Forward scattered particles was detected by Neutron Counter and Proton Counter. Forward scattered positive charged particles was swept to opposite direction of beam. Trajectory of these particles was measured by FDC1 just upstream of Ushiwaka magnet and these timing was measured by forward charged counters, CVC and PC.

Forward positive charged particle was identified from momentum reconstructed by the bending angle and β was calculated by forward charge counter. Forward neutral particles was detected by NC array. No hit in BVC and CVC was required to guarantee neutral particle just before NC. NC efficiency was estimated by liquid-H₂ target using $K^- p \rightarrow K^0 n$ reaction. Neutral particle rejection ratio by BVC and CVC was depend on beam condition, especially BVC that installed just upstream Ushiwaka magnet. So, we evaluated inefficiency of neutron by BVC and CVC using production run.

The $d(K^-, n) X$ and the $d(K^-, p) X$ identifying final state was finally convert to the cross section. The final state identification and conversion factor for count to cross section are explained.

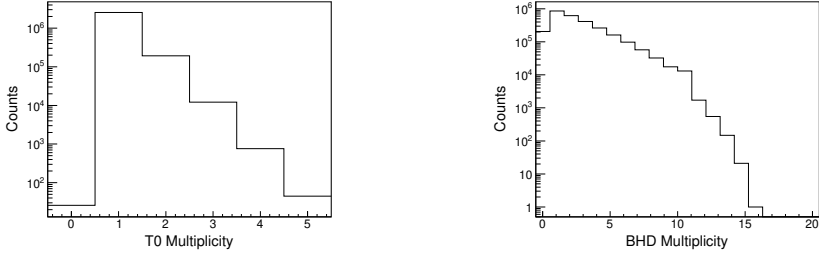


Figure 1.1: These figures show multiplicity of T0 and BHD counter.

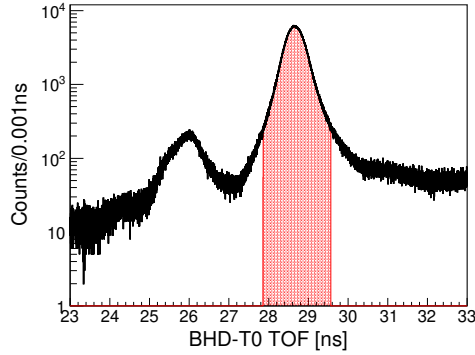


Figure 1.2: BHD-T0 time-of-flight with 7.7m flight length. Red hatched plot indicates acceptable region as a kaon.

1.2 Beam line

1.2.1 T0 and BHD analysis

T0 counter was installed at just upstream of CDC to define start timing of all detectors. BHD counter was installed to define beam particle by time-of-flight method with 7.7m flight-length. So, we require 1 hit of T0 counter. Fig[1.1] represents multiplicity of T0 and BHD counter. Because BHD multiplicity has many events is not 1hit, we don't require BHD 1hit. Fig[1.2] represents T0-BHD time-of-flight with on-line kaon trigger, which looks clear kaon peak around 29ns. Contamination of pion come from strange beam line or RF structure makes peak around 26ns. The red hatched region indicates selection of kaon beam.

1.2.2 Beam line changer

BLC1 and BLC2 was installed upstream and downstream of the D5 magnet, respectively to measure beam momentum unsing transfer matrix of D5 magnet. These are planer type drift chamber whose drift length was calculated using X-T map, which was integration of drift time. Track time of BLC was estimated from timing signals of pair plane due to constant drift

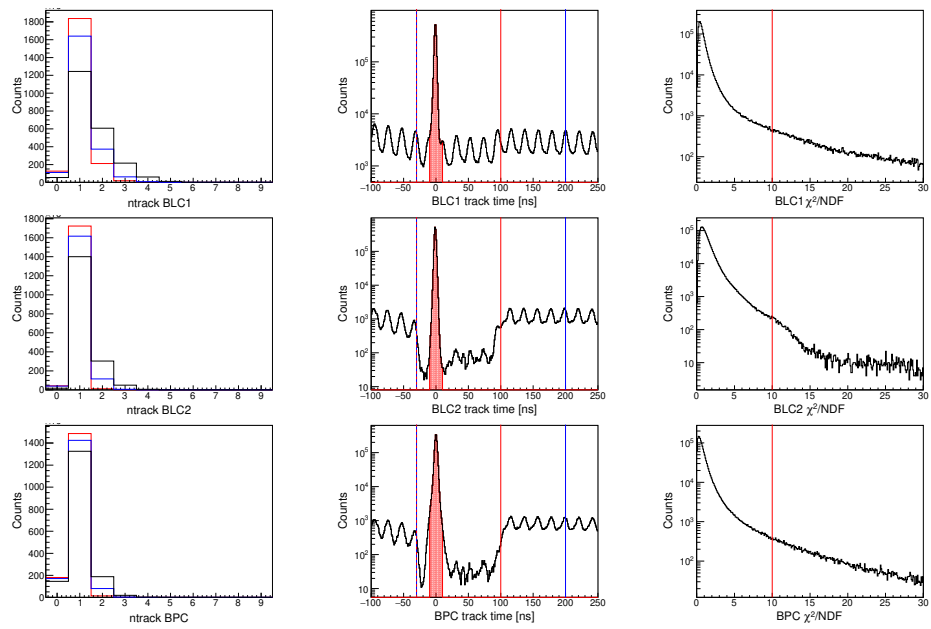


Figure 1.3: Left, middle and right figures shows number of tracks, track time and χ^2/NDF , repectively. Color plots in left figure indicate some time window. Right figure shows χ^2/NDF .

Above, middle and down figures represents about BLC1, BLC2 and BPC which was described after, respectively.

length. SX beam has RF-structure seems like middle figures of Fig1.3, so we select synchronization about beam which indicate red hatched region. Middle figures represents number of tracks, in which black, blue and red indicate time window, All, $-30 \sim 100$ [ns] and $-30 \sim 200$ [ns], respectively. We select 1track events in red time window selection to keep statistics. The right figures show χ^2/NDF distribution after 1track selection. We accepted $\chi^2/NDF < 10$ events as good track.

1.2.3 Beam momentum analyzer - D5 magnet

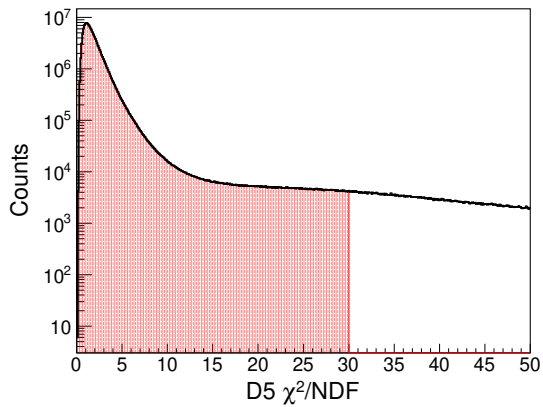


Figure 1.4: This figure shows connected trajectory of BLC1 and BLC2 using the D5 transfer matrix. The red hatched region represents acceptable region.

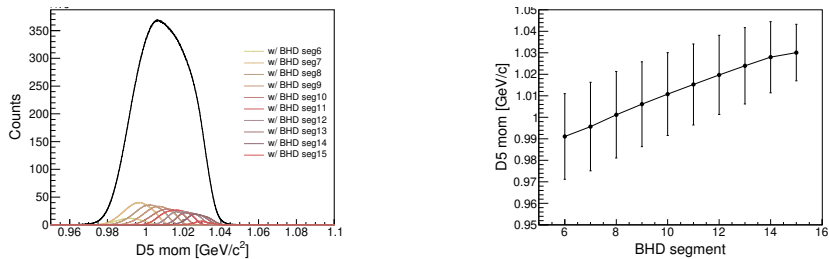


Figure 1.5: Left figure shows beam momentum. color plots indicate events tagged BHD segment in BHD multiplicity one events. Right figure represents center value of momentum as point and matching region as bar.

Beam particle momentum was calculated by connecting BLC1 track and BLC2 track using the transfer matrix of the D5 magnet. The χ^2/NDF of connection trajectory was shown as Fig1.4. We accept $\chi^2/NDF < 30$ events. Calculated beam momentum distribution is shown as Fig1.5, which is seen relation between beam momentum and BHD segments. So, we require

3σ level matching between beam momentum and BHD segment, which is shown as right figure.

1.2.4 BLC2-BPC matching

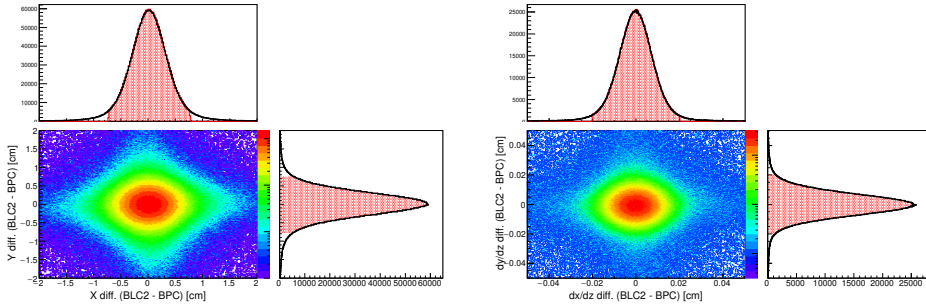


Figure 1.6: These figure indicate connection of the BLC2 and the BPC. Left figure shows about position matching at the center of these. Right figure shows about direction matching. The red hatched region was indicated acceptable region.

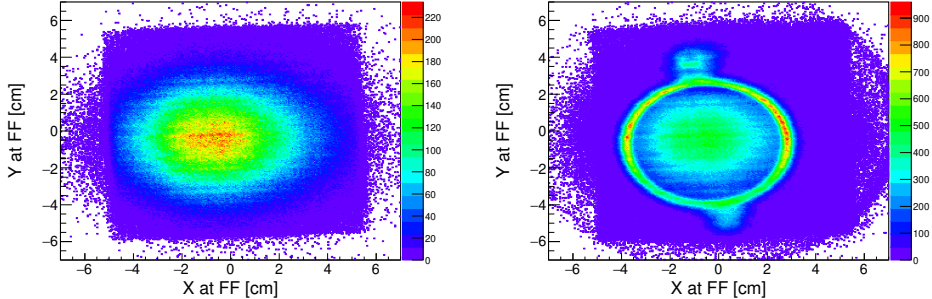


Figure 1.7: These figures shows beam profile at FF. Left figure shows about unbaised kaon trigger. Right figure shows about CDH2 hit trigger.

The BPC is same type drift chamber as BLC1/2, so the analysis of itself is same as BLC1/2, which is shown in Fig1.3. There is no magnet between the BLC2 and the BPC, so trajectories reconstructed by them should be successfully connected within multiple scattering and resolution. There are many materials between the BLC2 and the BPC, for example the T0, the AC, BPD and air, also direction (dx/dz or dy/dz) resolution affect on extracted position resolution. The z length ratio of these is $(BPC z)/(BLC2 z)=50.4\text{mm}/310\text{mm}\sim 1/6$, so extracted position resolution was almost decided by the BPC. On the other hand, materials was placed at just downstream of the BLC2 for example the T0 and the AC. These two effect was estimated almost same, so we evaluated position matching at the center of the BLC2 and the BPC as Fig1.6. We also require direction matching as

right figure. The BPC also define beam profile at the experimental target position as shown in Fig1.7. The profile required reaction at trigger level was clearly seen target cell. The red circle indicate acceptable region as effective kaon beam.

1.2.5 Irradiated kaon number

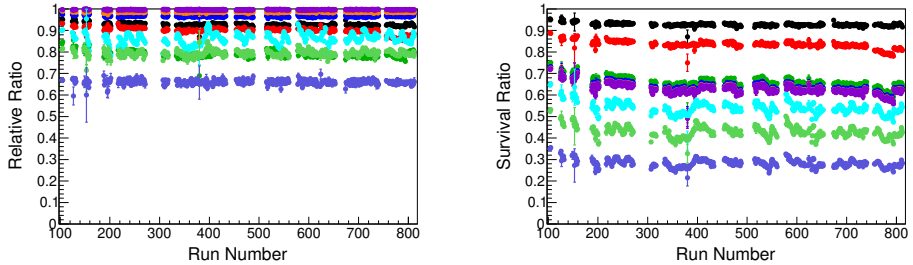


Figure 1.8: Left and right figure indicates run dependence of relative and survival ratio in MR Run78, respectively. Relative ratio means ratio against before condition. Survival ratio means ratio from all K/f trigger events.

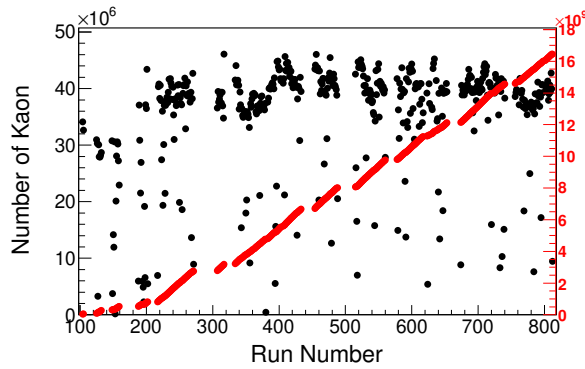


Figure 1.9: This figure shows kaon number irradiated on the liquid- D_2 target.

Kaon number at trigger level was counted by scaler DAQ, which includes incorrect event due to contamination of π , two particle, strange trajectory and convert or scattering on the beamline. We adopt many selection to avoid these events as described above. Below indicate items of beam line selection.

1. T0 1hit selection

2. T0-BHD TOF kaon selection
3. BLC1 1track selection
4. BLC2 1track selection
5. D5 momentum reconstruction
6. D5 and BHD matching selection
7. BPC 1track selection
8. BLC2 and BPC connection
9. Beam on target at FF

These values was shown in Fig1.8. Number of kaon irradiated on the liquid- D_2 target was evaluated with DAQ efficiency and trigger efficiency as luminosity ($L = N_{beam}N_{target}Eff_{DAQ}Eff_{trigger}$), which is evaluated each run as Fit1.9.

1.3 CDS

The CDS analysis was preformed below procedure

1. CDC tracking
2. Seach associated CDH (IH) hit.
3. Defining reaction vertex point and particle identification.
4. Re-fitting of CDC using β of particle

In this section, these analysis procedure is explained.

1.3.1 CDC tracking

The CDC tracking was performed in uniform magnetic field, so its track is helix track which was introduced by K.Fuji[40] as following equations.

$$x(\phi) = d_\rho \cos \phi_0 + \frac{1}{\rho} (\cos \phi_0 - \cos(\phi_0 + \phi)) \quad (1.1)$$

$$y(\phi) = d_\rho \sin \phi_0 + \frac{1}{\rho} (\sin \phi_0 - \sin(\phi_0 + \phi)) \quad (1.2)$$

$$z(\phi) = d_z - \frac{1}{\rho} \tan \lambda \dot{\phi} \quad (1.3)$$

where d_ρ is the distance of the helix from the origin point in the xy plane, d_z is distance of z direction, ϕ_0 is the azimuthal angle to z -axis, λ is elevation

angle and ρ is the inverse of the radius of the helix.

In this parametrization, charged particle momentum is represented as below,

$$\mathbf{p} = \frac{cB}{\rho} \begin{pmatrix} -\sin(\phi_0 + \phi) \\ \cos(\phi_0 + \phi) \\ \tan \lambda \end{pmatrix} \quad (1.4)$$

where c is the light velocity, B is strength of uniform magnetic field in the z direction.

Drift time convert to drift length using fifth order polynomial function which function was iteratively adjusted to minimize systematic shift. Fig1.10 shows drift time and drift length.

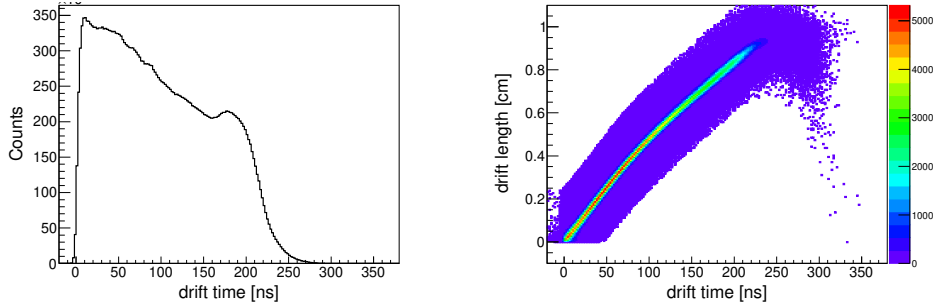


Figure 1.10: Left figure shows drift time distribution of CDC. Right figure shows relation of drift time and drift length.

1.3.2 CDH

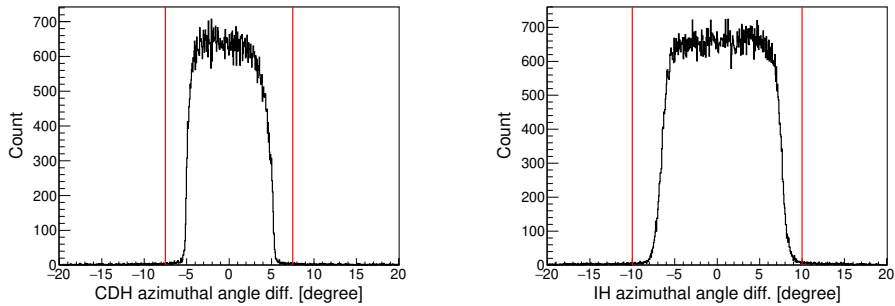


Figure 1.11: Left figure shows azimuthal angle difference the CDH hit segment and the CDC trackin. Right figure shows azimuthal angle difference the IH hit segment and the CDC tracking. The CDH and the IH segment size are $\pm 5^\circ$ and $\pm 7.5^\circ$, repectively. Acceptable region indicates red lines.

The CDH was installed outer side of the CDC and The IH was installed inner side of CDC. The CDH and IH hit position can defined exported

trajectory by the CDC like Fig1.11. The CDH and the IH have 36 and 24 segments, respectively which correspond to 10 degree and 15 degree of azimuthal angle. CDC track and CDH or IH hit within $\pm 7.5^\circ$ and $\pm 10^\circ$ are associated, respectively. Fig1.11 shows azimuthal angle matching of the CDC and the CDH and the IH.

The CDH timing information is used to identify of the particle. The flight length of the T0 to the CDH is calculated in two parts, one is the T0 to the reaction vertex point which was evaluated and next is the reaction vertex point to the CDH hit position.

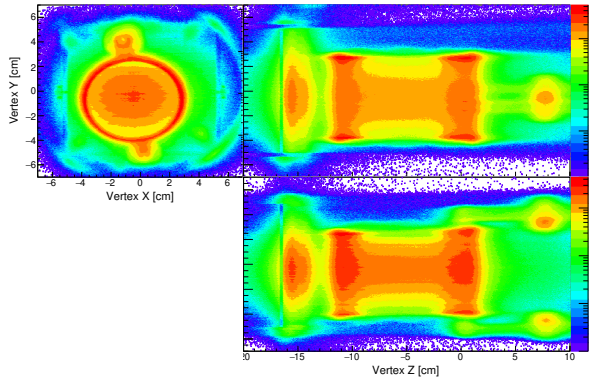


Figure 1.12: Reconstructed vertex point distribution by the BPC and CDC. Right figure shows about xy plane. Up figure and down figure of left side was shows yz plane and xz plane, respectively.

1.3.3 Vertex reconstruction

The reaction vertex point was calculated from the beam track by the BPC and the CDC tracks. First, the CDC track which gives the distance of the closest approach (DCA) was searched and the reaction vertex point was defined by closest point of the beam track. Fig1.12 shows reconstructed reaction vertex images. We used the target chamber with 6.8cm diameter PET whose image was clearly shown in xy plane figure. D_2 target transfer pipes placed parallel to the floor was shown at $z = 8\text{cm}$ in light side figures, also DEF counter installed just upstream of the target chamber was seen at about $z = -15\text{cm}$.

For evaluation of the vertex resolution, some projected histograms was made. The xy vertex resolution was evaluated at some range of z axis and target center of y as left figure of Fig1.13. The xy vertex resolution was evaluated about 1.4mm . The z vertex resolution was evaluated by the DEF counter using z axis projection histogram at $r < 3\text{cm}$. The z vertex resolution was evaluated about 7.0mm .

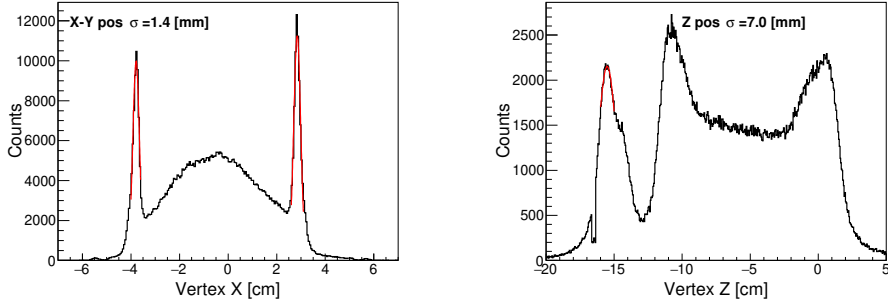


Figure 1.13: Left figure shows x axis projection at $y = 0\text{cm}$ and $z > -12.5\text{cm}$ to evaluate xy vertex resolution. Right figure shows z axis projection at $x^2 + y^2 < 3\text{cm}$ to evaluate z vertex resolution.

1.3.4 Particle identification

Decay particle was identified by the velocity calculated from the T0-CDH time-of-flight and the momentum evaluated from the curvature of magnetic field. The velocity β was calculated using below equation

$$\beta = \frac{1}{c} \frac{L_{\text{Vertex-CDH}}}{(TOF_{\text{CDH-T0}} - T_{\text{T0-Vertex}}^{\text{calc}})} \quad (1.5)$$

The $L_{\text{Vertex-CDH}}$ is the flight-length from the T0 to the CDH, which was calculated from line distance from the T0 to the reaction vertex and helix distance from the vertex to the CDH hit position. The $T_{\text{T0-Vertex}}^{\text{calc}}$ mean the calculated time from the T0 to the reaction vertex point using beam momentum analyzed by the D5 magnet with energy loss correction of the materials at beam trajectory. Decay charged particles identified by the mass square which calculated by the Eq.1.6 and the momentum.

$$m^2 = p^2 \times \frac{1 - \beta^2}{\beta^2} \quad (1.6)$$

1.3.5 Time walk correction of CDC

Start timing of CDC was of cause depend on the velocity of decay particle because reach time to drift area was depend on the velocity. Actually, the correlation between residual of CDC and the $1/\beta^2$ was seen in Fig1.15. The correlation was collected using time-walk collection like method by fitting with a function $p_0 + p_1x + p_2x^2 + p_3 \exp(p_4x)$. This collection was adopted wire-by-wire of the CDC. Fig1.15 represents all wire summed scatter plot. The figure after collection (right) seen almost no correlation.

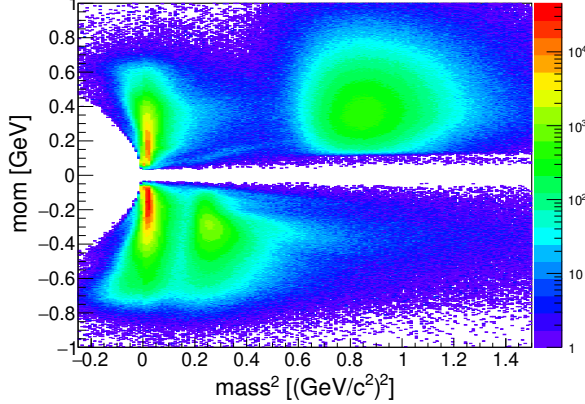


Figure 1.14: This figure shows scattered plot of mass square and momentum. Mass square was calculated by the Eq.1.6. Sign of the momentum means particle charge so, plus means positive charged particle and minus means negative charged particle.

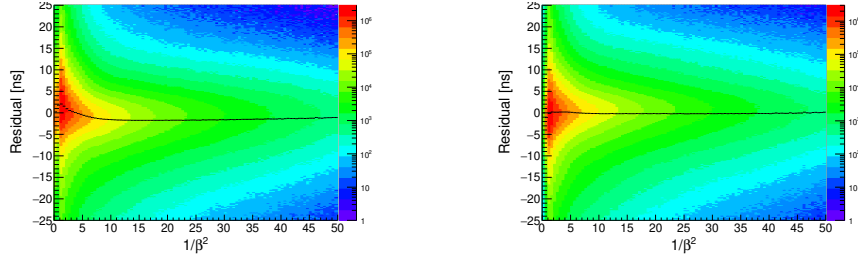


Figure 1.15: These figures show correlation between $1/\beta^2$ and residual convert to time using $dt-dx$ correction function. Left figure shows before time-walk collection. Right figure shows after time-walk collection.

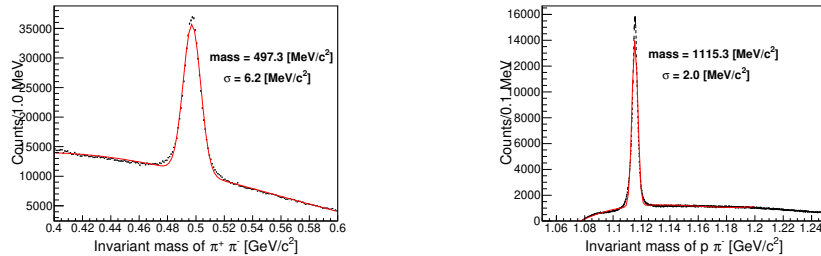


Figure 1.16: Left figure shows reconstructed K^0 from $\pi^+\pi^-$ detected by the CDS. Right figure shows reconstructed Λ from $p\pi^-$ detected by the CDS. Background function was evaluated by 5-th polynomial function.

1.3.6 Recunstructed hyperons by CDS

The K^0 and the Λ , well-known hyperons decay to $\pi^+ \pi^-$ and proton and π^- , respectively. These decayed particles can be identified and momentum was reconstructed by the CDS as shown in Fig1.16.

1.3.7 CDC efficeicny

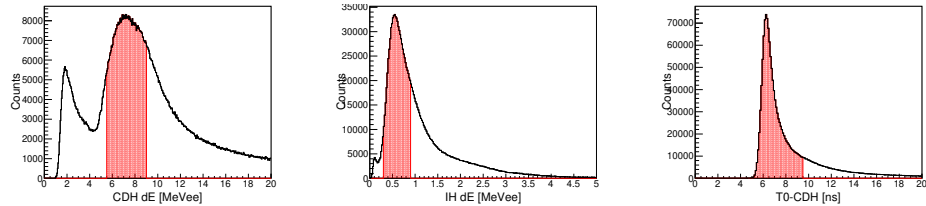


Figure 1.17: Trigger event selection for CDC efficeicny. left, center and right figures show CDH dE, IH dE and T0-CDH tof. Red hatched region indicates acceptable region as pass through MIP.

In MR-RUN68, the IH was installed at CDS which srounding the target cell. CDC efficeicny was estimated IH and CDH as trigger counter. Trigger events required specific energy deposite at CDH and IH to require MIP like particle and fast timing at CDH. IH do not use timming infomation because sigle read-out and bad time resolution. CDH and IH hit in same side, azimuthal angle difference within 45° , was required for trigger events. CDC efficeicny was estimated whether can be right trajectory reconstructed. Right trajectory was judged within a half of hodoscope size. We estimated CDC efficeicny at $97.7 \pm 0.4\%$ which error was evaluated by fractuation of CDH trigger segment.

1.4 Forward counter

In this section, the PC and the NC analysis procedure was explained. The start point was determined by the closest beam track and the CDS track combination. So neutral particles was not bended by the magnetic field, these flight length was calculated as straight line from the reaction vertex to hit position of the NC. On the other hand, forward positive charged particles was bended by the Ushiwaka, trajectory upstream Ushiwaka was determined by the reaction vertex and the FDC1 track and the trajectory was extrapolated to the PC hit segment. And detected particle selection for the final event sample identified the specific reaction was discribed. First, about forward proton analysis was explained and next is about forward neutron analysis.

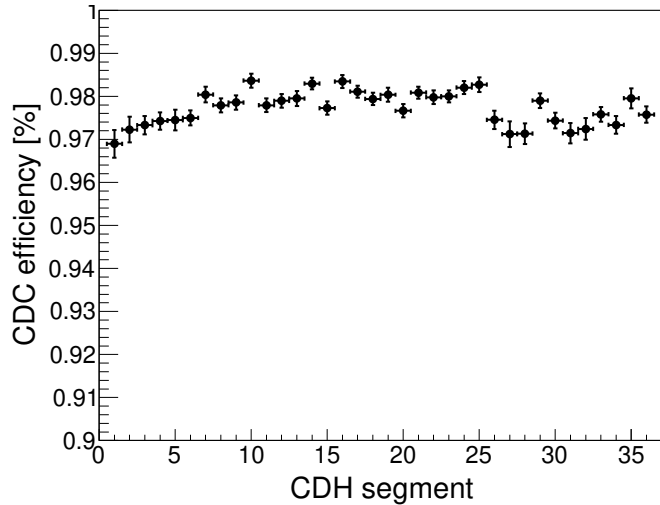


Figure 1.18: This figure plotted CDC efficiency about each CDH trigger segment.

1.4.1 Forward proton analysis

Forward proton was bended by the Ushiwaka magnet and fired the PC, so the flight length of forward charged particle was depend on the momentum and scattered angle. The flight length was evaluated from the reaction vertex point, position at just upstream of the Ushiwaka magnet measured by the FDC and counter hit position. The trajectory was calculated by the third order Rungge-Kutta method with magnetic field map. The field map was calculated by the Opera which is finite element method software and absolute value was scaled by measured value. The velocity (β) was calculated using the TOF method. The flight time was calculated using same method of decayed particle measured by the CDS. Fig.1.19 shows scattered plot of mass-square and momentum. The momentum was estimated from the bending angle and mass-square was calculated from the velocity and momentum. Events whose $m^2 > 0.5[(GeV/c^2)^2]$ are accepted as the proton. Fig.1.20 shows the $d(K^-, p)$ missing mass.

The momentum was measured by the TOF method, although flight length was function of the scattered angle and the momentum. The position just above the Ushiwaka magnet was measured by the FDC1 and the trajectory was extrapolated to the fired counter. The trajectory of the forward scattered charged particle was calculated by the third order Rungge-Kutta method using the magnetic field calculated by the Opera[41].

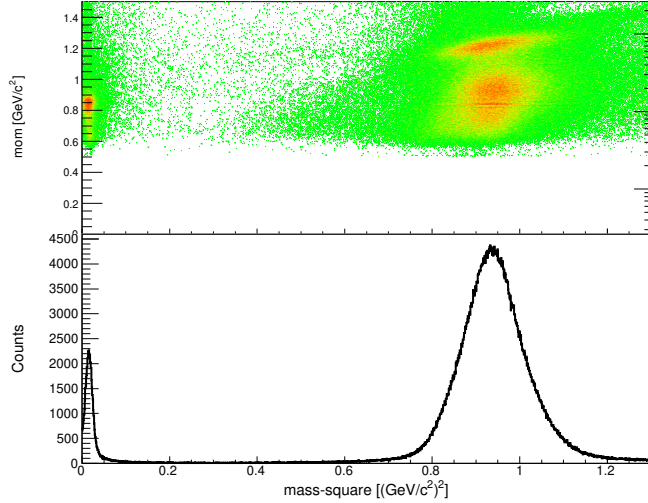


Figure 1.19: This figure shows scattered plot mass-square and momentum of forward scattered positive charged particles and horizontal axis projection (down figure). The π^+ peak is seen around $m^2 \sim 0.02[(\text{GeV}/c^2)^2]$ and the proton peak is seen around $m^2 \sim 0.9[(\text{GeV}/c^2)^2]$

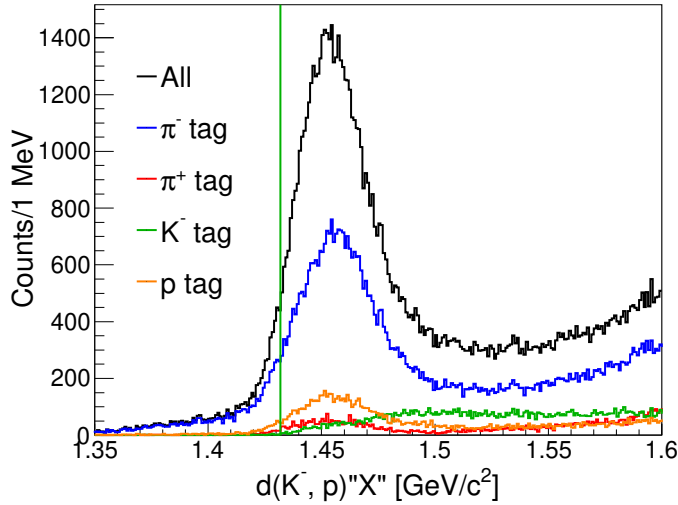


Figure 1.20: This figure shows $d(K^-, p)^"X"$ missing mass spectra. Black plot indicates whole data and color plots indicates CDS particles tagged data. These plots was adopted time offset turning using missing mass of $d(K^-, pK^-)^"p"$ data.

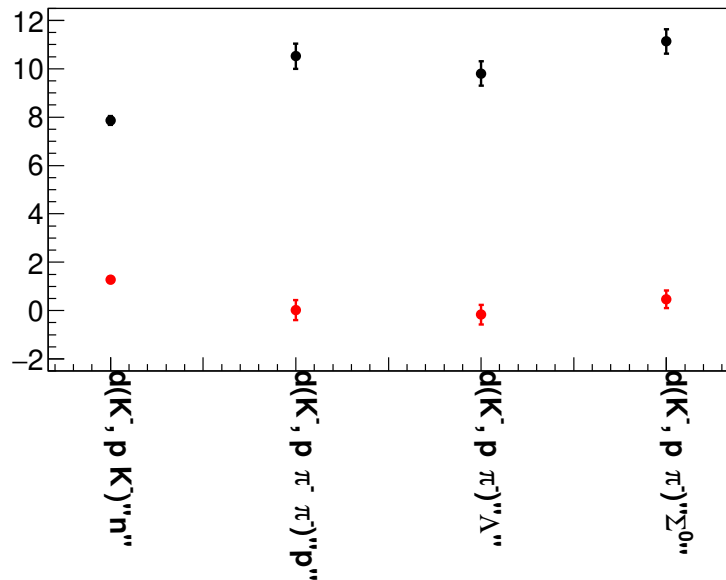


Figure 1.21: This graph indicates difference of peak position of missing masses which was expected as well-known particle. Black plots indicate data that calibrated using pion through run. Red plots indicate data after calibration using these missing masses.

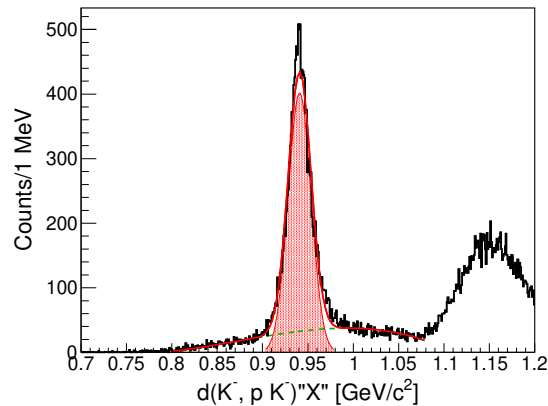


Figure 1.22: This figure shows $d(K^-, p K^-)''X''$ missing mass spectrum in forward proton and K^- tagged events. Red line is whole fitting result and red hatch indicates fitting gaussian. Background was estimated 3rd order polynomial function which indicates green dotted line.

1.4.2 Time offset turning

Time offset was calibrated using special data at first. In these data, the $1\text{GeV}/c$ pion was injected with various Ushiwaka magnet value to irradiate all segments of the CVC and the PC. These data was accumulated by unbaised trigger. Time offsets were calculated from the trajectory and velocity, which is almost light velocity, of pion.

The time offset was shifted due to ambiguity of the alignment which was seen in the missing masses of well-known particles, $d(K^-, pK^-)''n''$, $d(K^-, p\pi^-\pi^-)''p''$, $d(K^-, p\pi^-)''\Lambda''$ and $d(K^-, p\pi^-)''\Sigma^0''$. These shift was calibrated using the missing masses. In this calibration, the beam momentum and decay particles momentum detected by the CDS was fixed and time offset was determined to give correct masses. Fig1.21 indicates difference of fitting mean value from the PDG values. Black points show about before calibration and red points show about after calibration. Differences from PDG value of after calibration are within $2\text{MeV}/c^2$. $d(K^-, pK^-)''n''$ peak was clearly seen as Fig1.22. Another missing masses are described Sec1.4.4.

1.4.3 Consistency check using invariant mass of $\Lambda\pi^-$ by the CDS

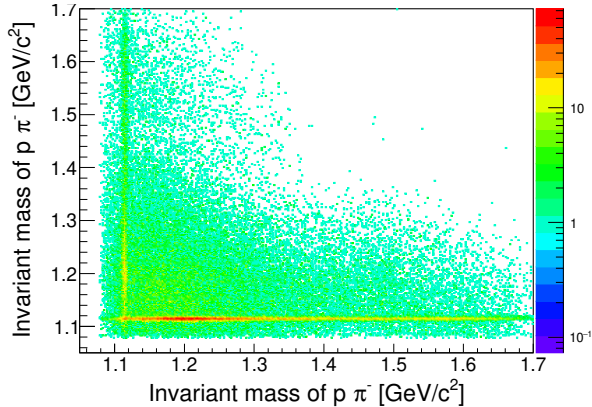


Figure 1.23: This figure shows 2-D plot of $p\pi^-$ invariant masses. Horizontal axis represents about near DCA pair and vertical axis represents about the other pair.

In events which detect two π^- and proton by the CDS, $d(K^-, \Lambda\pi^-)''p''$ events was observed. These events can be used to confirm accuracy of missing mass of $d(K^-, p)$. Fig1.23 shows scattering plot invariant mass of $p\pi^-$. Fig1.24 shows missing masses of $d(K^-, \Lambda\pi^-)''X''$ which is clearly seen $d(K^-, \Lambda\pi^-)''p''$ with charge trigger.

Fig1.25 represents relation of $\Lambda\pi^-$ invariant mass and missing mass of $d(K^-, p)$. Difference of missing mass of $d(K^-, p)$ and invariant mass of $\Lambda\pi^-$

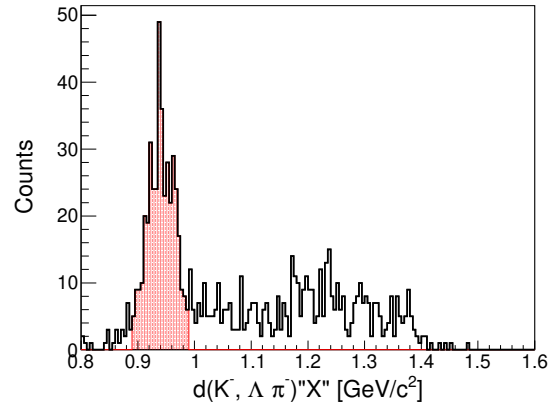


Figure 1.24: This figure shows missing mass of $d(K^-, \Lambda\pi^-)$ whose Λ and π^- was detected by the CDS. Red hatched region indicates selection region as missing proton.

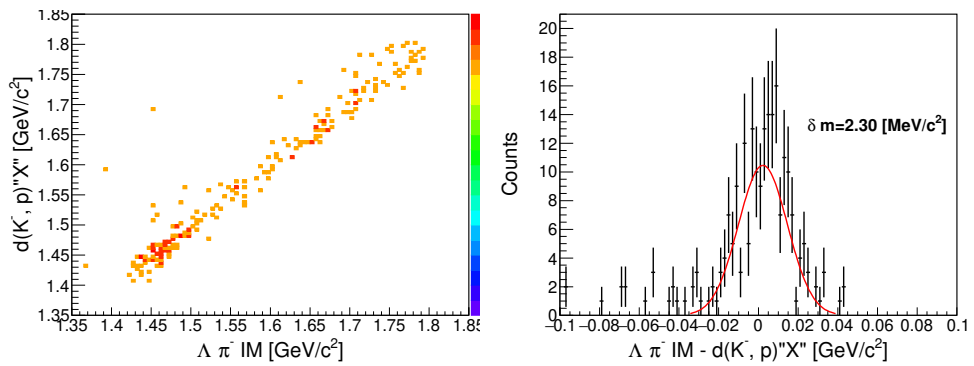


Figure 1.25: These figure indicate relation of $d(K^-, p)''X''$ and $\Lambda\pi^-$ invariant mass in events which detect Λ and π^- by the CDS and p by the PC/CVC. Left figure shows scatter plot and right figure represents subtraction distribution from invaraint mass to $d(K^-, p)''X''$.

was estimated at $2.3 MeV/c^2$.

1.4.4 $d(K^-, p)\pi^- \Lambda$ and $d(K^-, p)\pi^- \Sigma^0$ identification

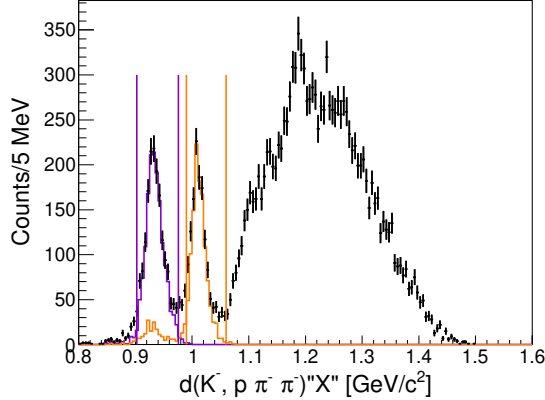


Figure 1.26: This figure shows the missing mass of $d(K^-, p\pi^-\pi^-)$. Orange and purple lines indicate selection region as missing p and $p\pi^-$, respectively. $d(K^-, p\pi^-)\Sigma^0$ and $d(K^-, p\pi^-)\Lambda$ tagged events are drawn orange and purple plot in same figure.

$d(K^-, p)\pi^- \Sigma^0$ and $d(K^-, p)\pi^- \Lambda$ can decay as follow

$$K^- d \rightarrow p\pi^- \Sigma^0 \rightarrow p\pi^- \gamma \Lambda \rightarrow p\pi^- \pi^- \gamma p \quad (1.7)$$

$$K^- d \rightarrow p\pi^- \Lambda \rightarrow p\pi^- \pi^- p \quad (1.8)$$

These two final state are different only γ . These two modes was searched in events that detected proton and $2\pi^-$ by the forward counter and the CDS respectively that event selection was also required some offline condition, synchronizing beam timing and energy deposite of the CDH, to avoid contaminate fake events which was explained in Sec??. Fig1.26 plotted $d(K^-, p\pi^-\pi^-)X$ missing mass in which $d(K^-, p\pi^-\pi^-)p$ and $d(K^-, p\pi^-\pi^-)p\gamma$ peaks was clearly seen. $d(K^-, p\pi^-)\Lambda$ and $d(K^-, p\pi^-)\Sigma^0$ tagged spectra was plotted in the same figure. Fig1.27 shows scatter plot of $d(K^-, p\pi^-)X$ in which $d(K^-, p\pi^-)\Lambda$ and $d(K^-, p\pi^-)\Sigma^0$ locus were clearly seen. Same scatter plots tagged $d(K^-, p\pi^-\pi^-)p$ and $d(K^-, p\pi^-\pi^-)p\gamma$ were shown in Fig??. There were no events other than Λ and Σ^0 in left and right figure respectively. These events were plotted as that a $p\pi^-$ pair giving near PDG value regarded true combination. Then that becomes Fig1.29 which was used for time calibration of the PC and the CVC. The $d(K^-, p\pi^-)\Lambda$ tagged events have no events other than $d(K^-, p\pi^-\pi^-)p$ peak. The $d(K^-, p\pi^-\pi^-)p$ tagged events have no events other than $d(K^-, p\pi^-)\Lambda$ peak. The $d(K^-, p)\pi^- \Lambda$ mode is identified by both missing mass, so we

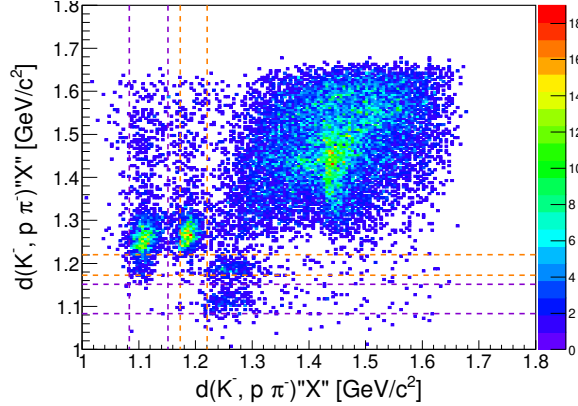


Figure 1.27: This figure shows the scatter plot of the $d(K^-, p\pi^-)$ missing masses in the p and two π^- detected events. Horizontal axis represents nearer DCA π^- and virtual axis represents other one. Orange and purple lines indicate selection region as $d(K^-, p\pi^-)\Sigma^0$ and $d(K^-, p\pi^-)\Lambda$, respectively.

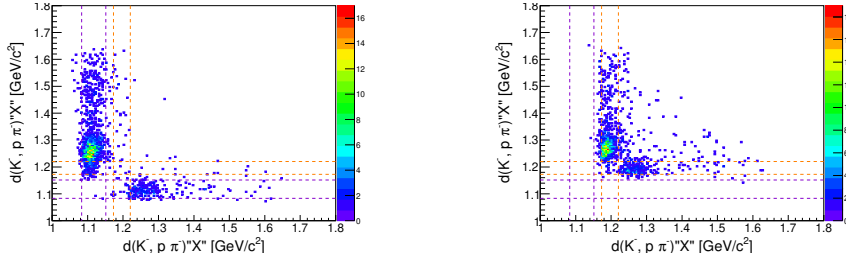


Figure 1.28: These figures shows same figure of Fig?? excepting $d(K^-, p\pi^-\pi^-)$ tag. Left figure shows $d(K^-, p\pi^-\pi^-)p$ tagged events and right figure shows $d(K^-, p\pi^-\pi^-)p\gamma$ tagged events.

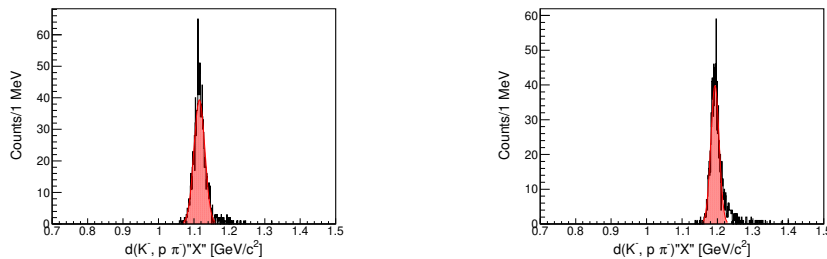


Figure 1.29: This figure indicate 1 dimensional plots of Fig1.28. Only near pair from PDG mass was filled histogram. These mass is Λ and Σ^0 left and right respectively.

Table 1.1: Summary table of $d(K^-, p)$ scaling parameters

| Component | value | error | value | error |
|---|-------|--------|-----------------------|--------|
| 2478.1 +- 80.6016 Luminosity (/ μb) | 2478 | 81 | | |
| Target Length (cm) | | | 10 | |
| Target density [g/cm^3] | | | 0.1624 | 0.0014 |
| Number of Kaon | | | 2.05×10^{10} | |
| Survival ratio of K^- | | | 0.336 | 0.0001 |
| DAQ live ratio | | | 0.821 | 0.0001 |
| Trigger efficiency | | | | |
| $K \otimes CDH1$ | | | 0.9527 | 0.0003 |
| Charge | | | 0.9559 | 0.0004 |
| Efficiency of the CDC | 0.977 | 0.04 | | |
| Acceptance of the PC/CVC (msr) | 21.0 | 0.0002 | | |
| Efficeincy Of the FDC1 | 0.967 | 0.007 | | |

adopt both selection. The $d(K^-, p)''\pi^-\Sigma^0$ mode is the same. $d(K^-, p)''\pi^-\Sigma^0''$ and $d(K^-, p)''\pi^-\Lambda''$ spectra were shown in Fig1.30.

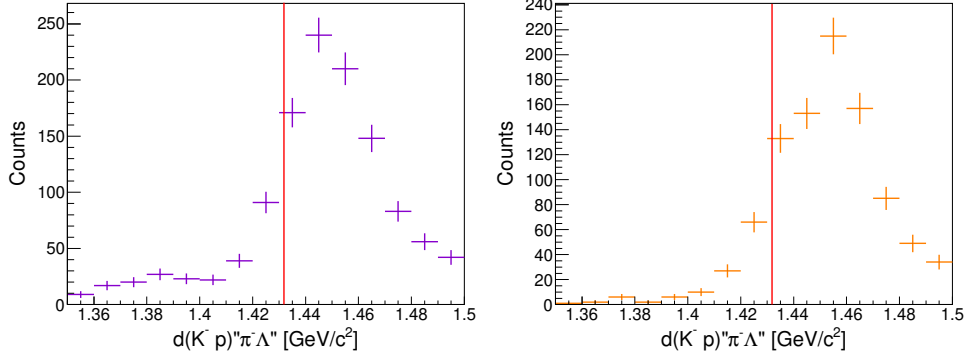


Figure 1.30: Left figure shows $d(K^-, p)''\pi^-\Lambda''$ and Right figure shows $d(K^-, p)''\pi^-\Sigma^0''$

1.4.5 Conversion factor of the $d(K^-, p)$

$d(K^-, p)''X''$ spectrum can be converted from counts to the differential cross section ($\frac{d^2\sigma}{d\Omega dm}$) excepting the acceptance of the the CDS that is depend on the reaction. The parameters was used for the conversion were summarized in Table1.1.

First one is luminosity which was consist of number of target, number of irradiated kaon, DAQ live rate, trigger efficeincy. The number of target was defined from length of fiducial volume (10cm) and target density which was evaluated from measured tempature. The number of irradiated kaon was

defined by correcting kaon number counted up by the scaler DAQ by ratio of true kaon in kaon trigger which was described in Sec1.2. About DAQ live rate and trigger efficiency were described in Sec???. The luminosity was evaluated run-by-run. In the table, these items were represented value weighted by data statistics as typical value.

Next is about the CDS which was CDC efficiency described in Sec1.3.7. Acceptances of CDS were estimated and corrected by the Monte Carlo simulation data. These evaluations were described in individual section for each reactions.

Last about forward detectors for forward scattered charge particle. Acceptance of PC/CVC was estimated using the Monte Carlo simulation using $d(K^-, p)$ reaction.

1.4.6 $d(K^-, p)\pi^- \Sigma^0$ and $d(K^-, p)\pi^- \Lambda$ cross section

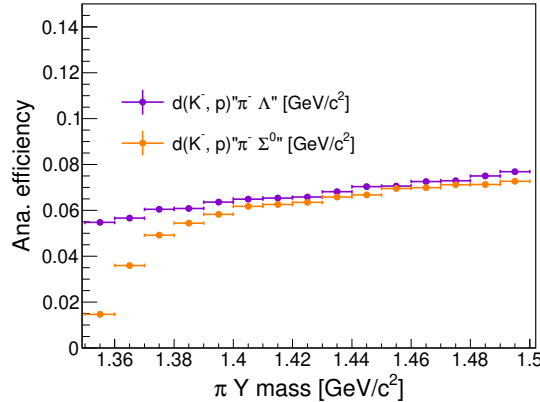


Figure 1.31: This figure shows acceptances of the $d(K^-, p)\pi^- \Sigma^0$ and the $d(K^-, p)\pi^- \Lambda$ which was estimated by the Monte Carlo simulation.

The $d(K^-, p)\pi^- \Sigma^0$ and the $d(K^-, p)\pi^- \Lambda$ spectra was converted to the corss section to collected acceptance. For this, we performed the Monte Carlo simulation using geant4 toolkit which was described in detail in Sec???. In this simulation, proton was generated at forward angle which is within $\theta < 8$ degree. Since this simulation's purpose was evaluation of the CDS acceptance, we used proton pass through PC/CVC as denominator events. We estimated effective events to adopt same analysis procedure to Monte Carlo simulations data, so the efficeincy includes analysis efficiency which is PID selection of the CDS and each gete for particles and so on. For the acceptance estimation of these reactions, we simulated $K^- d \rightarrow \pi^- \Sigma^0 p_{forward}$ and $K^- d \rightarrow \pi^- \Lambda p_{forward}$ reactions. In this simulation, masses of $\pi^- \Sigma^0 / \pi^- \Lambda$ were adopted flat distribution for same statistics in region of interest.

We obtain corss sections of the $d(K^-, p)\pi^- \Sigma^0$ and the $d(K^-, p)\pi^- \Lambda$

to be corrected by acceptance. Fig1.32-1.33 show obtained corross sections. In these figures, statical errors which is dependent error for each bins was indicated using boxes and errors which was convolved error of conversion factor parameters that is common in all bins was indicated as error bars.

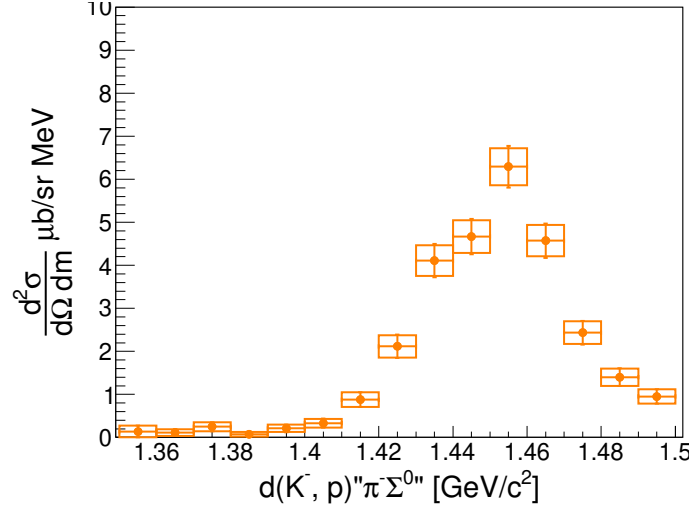


Figure 1.32: The cross section of $d(K^-, p)''\pi^- \Sigma^0$ mode.

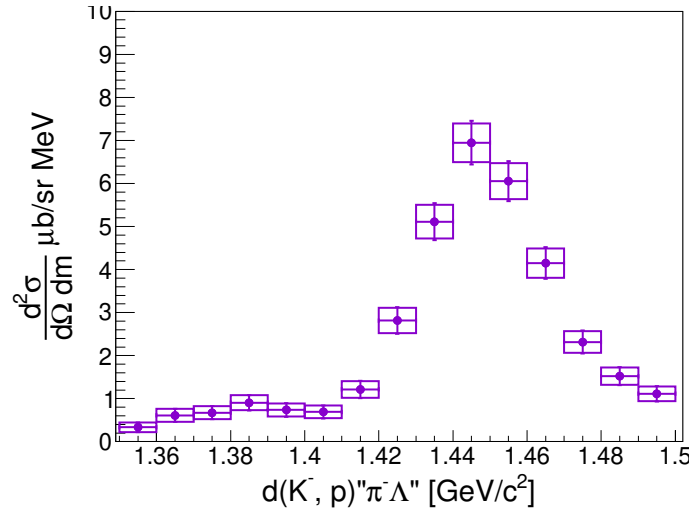


Figure 1.33: The cross section of $d(K^-, p)''\pi^- \Lambda^0$ mode.

1.4.7 Neutron counter

Nutral particles scattered forward direction was deteceted by the NC. Charged particle was rejected by the CVC, which was installed just upstream of the

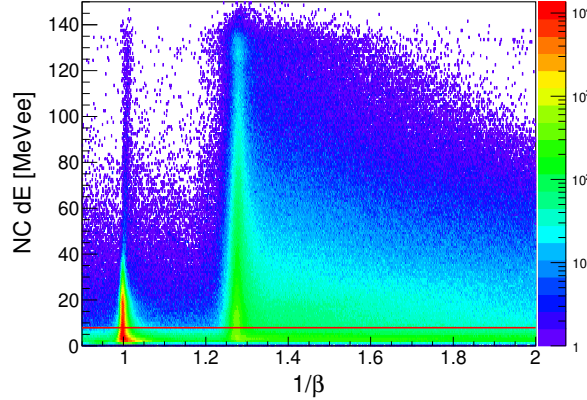


Figure 1.34: This figure show scattered plot of $1/\beta$ and energy deposit. γ -ray events was observed at $1/\beta = 1$. locus at $\beta = 1.3$ was correspond to quasi-elastic scattering events.

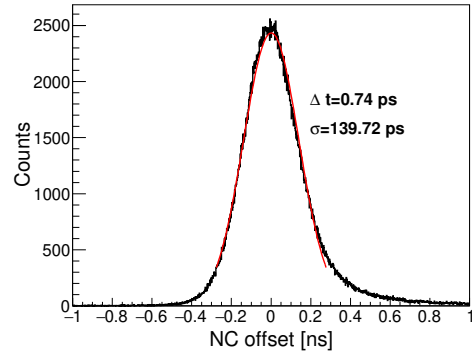


Figure 1.35: This figure shows γ -ray peak in $1/\beta$ distribution with 8 MeVee offline threshold. Fitted gaussian was shown as red slope and mean and σ value was indicated at same figure.

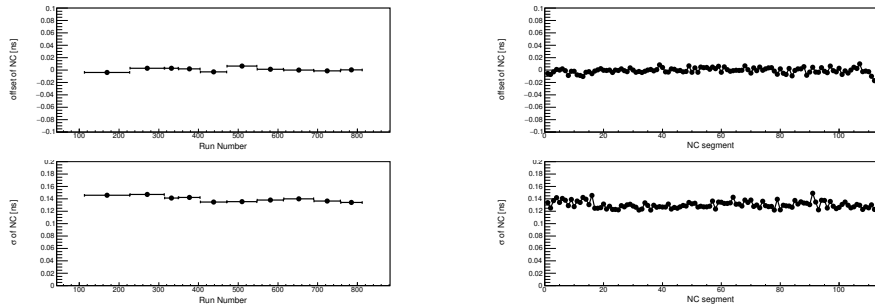


Figure 1.36: These figures show stability of the NC performance. Above figure indicates the fluctuation of the γ -ray peak and down figure indicates the time resolution of the NC. Right figure and left figures show run dependency and segment dependency, respectively.

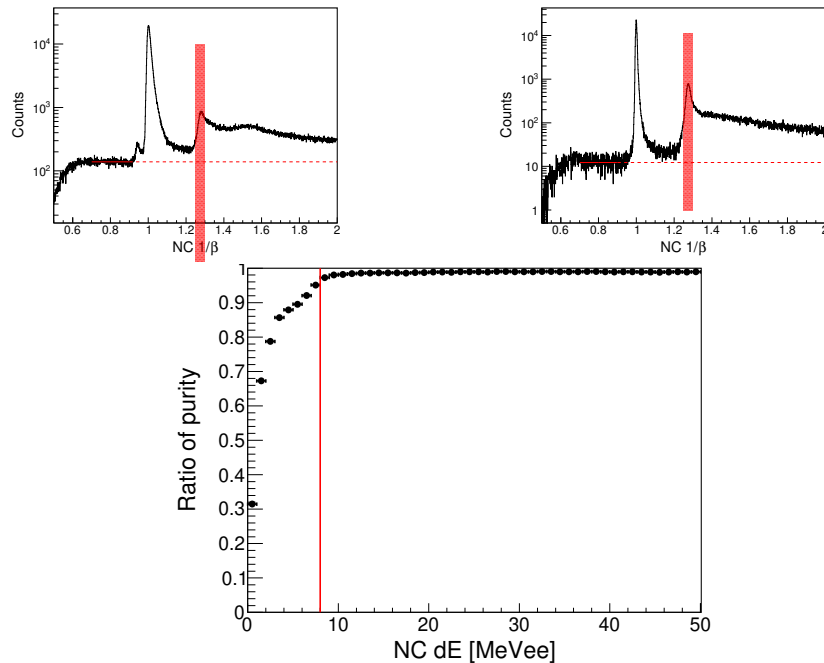


Figure 1.37: Up figures shows $1/\beta$ distribution with specific dE range. Left figure and right figure show about $dE = 2 \sim 3 \text{ MeVee}$ and $dE = 8 \sim 9 \text{ MeVee}$, respectively. Red line indicate background level which estimated at $1/\beta = 0.7 \sim 0.9$. Red hatch region indicate integral range as signal. Down figure shows dE dependency of the ratio of signal and background. Red line indicates online threshold level($dE = 8 \text{ MeVee}$).

NC, and the BVC which was installed upstream of beam sweeping magnet. Start timing was calculated from the T0 timing and flight time of the T0 to the vertex point. Time-of-flight was calculated from the NC timing and start time. X position was decided from counter position and y position was evaluated to convert subtracted signals of up and down using effective light velocity which was evaluated ${}^{90}\text{Sr}$ source measurement with some points. Scatted plot of $1/\beta$ and energy deposit was shown in Fig1.34. The NC was set the threshold of signal at 1/10 of MIP. Low energy deposit has many background which was estimated in unphysical region, $1/\beta = 0.7 \sim 0.9$. And purity of neutron events was estimated using quasi-elastic events ($1/\beta 1.25 \sim 1.30$). These figures was shown in Fig1.37. The purity of the NC was saturated at 8MeVee , so we adopted this value as offline threshod.

In this condition, the NC time resolution was estimated at 140 ps using γ -ray peak as Fig1.35. Fig1.36 was shows stability of the NC dureing production run and segment dependency.

$d(K^-, n)$ missing mass spectrum was shown in Fig1.38 with the CDS particles tagged.

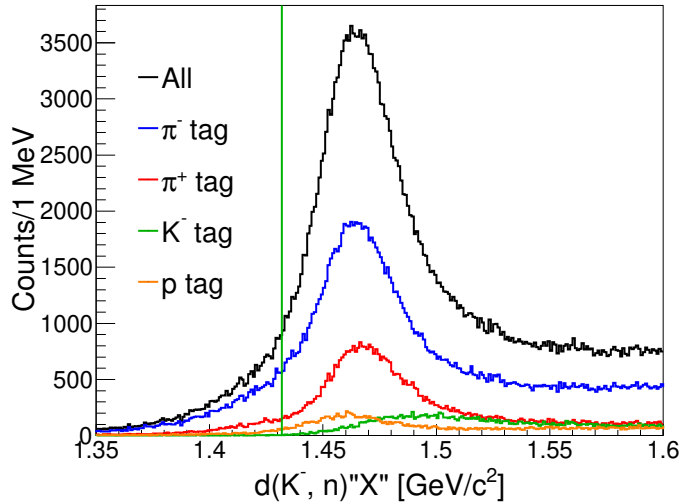


Figure 1.38: This figure shows $d(K^-, n)''X''$ missing mass. Black plot indicates all data and color plots indicate data with the CDS particle tag.

1.4.8 NC efficiency estimation

NC efficiency was estimated by $K^-d \rightarrow K^0n$ reaction using liquid- H_2 target, which shows Fig[1.39]. $p(K^-, \pi^+\pi^-)''n''$ was selected by read hatched region. In this final state, these three processes were expected.

1. $K^-p \rightarrow K^0n$

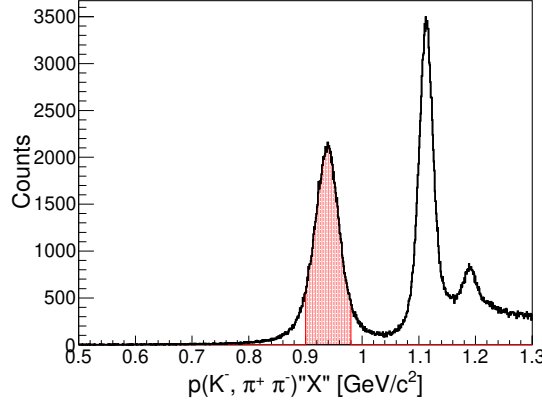


Figure 1.39: This figure shows $p(K^-, \pi^+ \pi^-)X'$. π^+ and π^- were detected by CDS. A peak around $1.1\text{GeV}/c$ was due to $d(K^-, \pi^+ \pi^-)\Lambda'$.

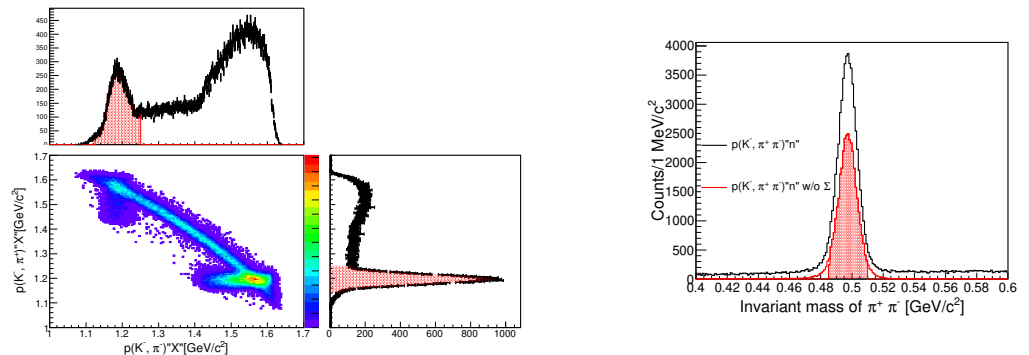


Figure 1.40: This figures show $K^- p \rightarrow \pi^+ \pi^- n$ event decompisition. Left figure shows scatter plot of $d(K^-, \pi^+)X'$ and $d(K^-, \pi^-)X'$, which clealy seen " Σ^- " and " Σ^+ ", respectively. The red hatched region indicate these selection. Right figure shows

2. $K^- p \rightarrow \pi^+ \Sigma^-$

3. $K^- p \rightarrow \pi^- \Sigma^+$

Reaction 2.3. were rejected by $p(K^-, \pi^\pm)''\Sigma^\pm$, as shown in 1.40. Also, K^0 reconstruction was confirmed and correct momenta reconstruction of π^+ and π^- was guaranteed.

Hit position at NC can be reconstructed from $p_n = p_{beam} - p_{K^0}$ and vertex position which shows in Fig 1.41. We adopt denominator event is no hit in CVC and BVC to evaluate intrinsic the NC efficiency. Because neutron pass through point fluctuate by the momentum resolution, we measured the NC efficiency using some selection of neutron pass through region. The efficiency almost was saturated at the setting is -20cm small from the NC size, so we estimated the NC efficiency at this setting. We evaluated the intrinsic NC efficiency at $31.7 \pm 1.6\%$.

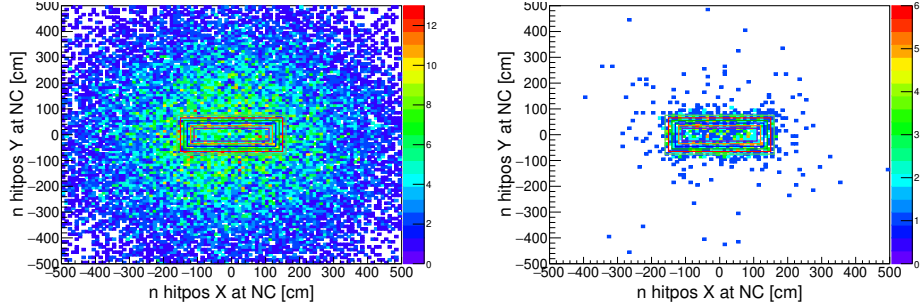


Figure 1.41:

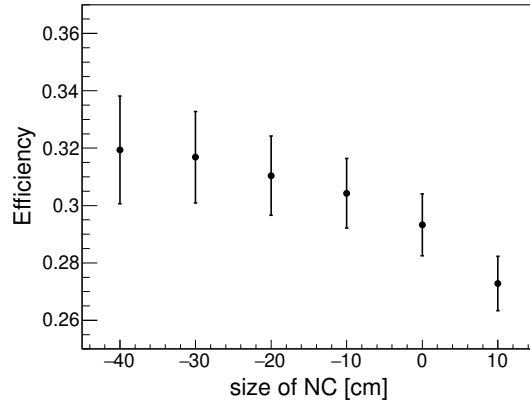


Figure 1.42:

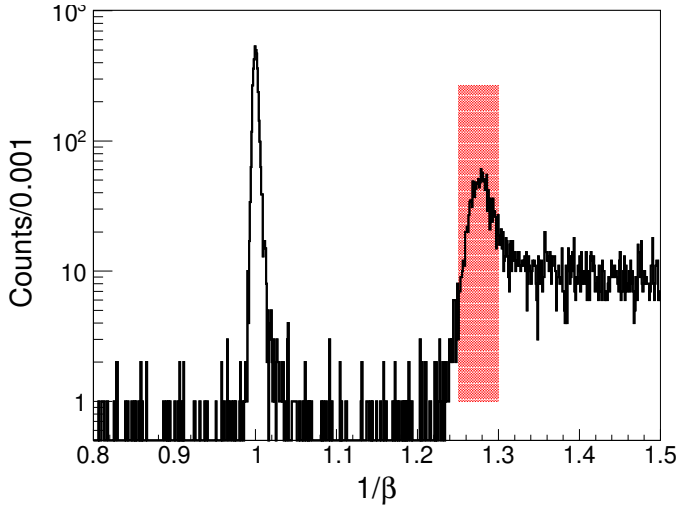


Figure 1.43: This figure shows $1/\beta$ spectrum by layer 2~7 of the NC with NC layer 1 veto in $K \otimes CDH2$ trigger. Quasi-elastic peak was seen around $\beta = 1.27$. Red hatched region indicate acceptable region as quasi-elastic neutron.

1.4.9 Neutron overkill by the BVC/CVC

The event neutron fired the NC and the BVC or the CVC can not accumulated as ntral event. Especially, the BVC maybe was fired by pill up particles and so on. Because this is strongly depend on beam condition, overkill ratio was evaluated each the MR-RUN operation. In MR-RUN78, denominator events use prescaed $K \otimes CDH2$ trigger. True neutron was identified by the NC. Layer 1 of neutron counter was used as charge veto counter, so no fire in NC layer1 guaranteed neutral particle. Fig.1.43 indicate $1/\beta$ spectrum by NC layer 2~7 in $K \otimes CDH2$ trigger. Overkill ratio was evaluated using quasi-elastic events which was seen at $1/\beta = 1.25 \sim 1.3$. So, red hatced region was used as trigger event for overkill. We estimated neutron overkill ratio by BVC or CVC at $8.1 \pm 0.7\%$.

1.4.10 High order correction for dE

The NC time walk effect was calibrated by γ conversion events around the target system which was seen in Fig1.34. So neutron made large energie deposit events, γ events was not enough for calibration of large energy deposit correction which was seen in $d(K^-, n\pi^+\pi^-)"n"$ events that is described after section. Fig1.44 shows these effect which was convert to time offset giving true PDG value of neutron. This effect was calibrated using 3rd polynomial function which is shown in same figure.

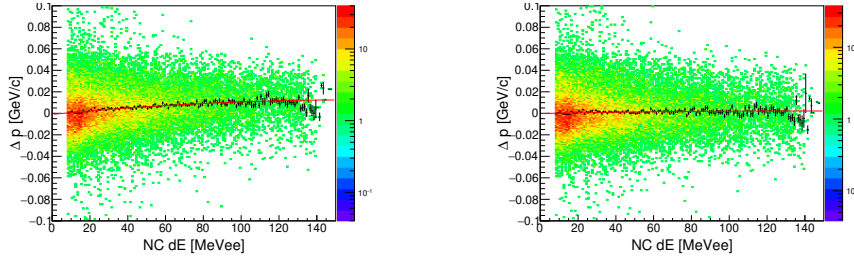


Figure 1.44: These figures show Δp which was calculated by given PDG value of neutron mass. Left figure represents before calibration and right figure represents after calibration.

1.4.11 $d(K^-, n)$ scaling factor

$d(K^-, n)"X"$ spectrum can be converted from counts to the differential cross section ($\frac{d^2\sigma}{d\Omega dm}$) excepting the acceptance of the the CDS that is depend on the reaction. The parameters was used for the conversion were summarized in Table1.2.

First one is luminosity which was consist of number of target, number of irradiated kaon, DAQ live rate, trigger efficency. The number of target was defined from length of fiducial volume (10cm) and target density which was evaluated from measured tempature. The number of irradiated kaon was defined by correcting kaon number counted up by the scaler DAQ by ratio of true kaon in kaon trigger which was described in Sec1.2. About DAQ live rate and trigger efficiency were described in Sec???. The luminosity was evaluated run-by-run. In the table, these items were represented value weighted by data statistics as typical value.

Next is about the CDS which was CDC efficiency described in Sec1.3.7. Acceptances of CDS were estimated and corrected by the Monte Carlo simulation data. These evaluations were described in individual section for each reactions.

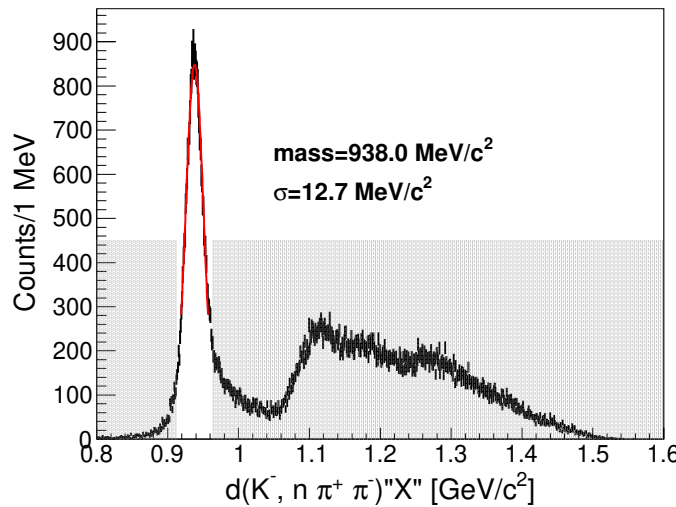
Last one is about the NC which was consists of acceptance and efficiency. The efficiency of the NC was further decomposed to intrinsic one and overveto by the CVC and the BVC that was described in Sec1.4.8. The acceptance of the NC was estimated from the NC position and the error was evaluated from difference of the first layer and the last layer of the NC.

1.4.12 $K^-d \rightarrow n\pi^+\pi^-n$ reactions

$K^-d \rightarrow n\pi^+\pi^-n$ final state was identified in events $n_{forward}$ and $\pi^+\pi^-$ detected by the NC and the CDS respectively which spectrum was shown in Fig1.45. These event selection was adopted offline analysis at seme as $d(K^-, p\pi^-\pi^-)$ analysis which discribed at ???. $d(K^-, n\pi^+\pi^-)"n"$ events had contamination from materials between rection vertex to the NC. We

Table 1.2: Summary table of $d(K^-, n)$ scaling parameters

| Component | value | error | value | error |
|-----------------------------|-------|-------|-----------------------|----------------------|
| Luminosity ($/\mu b$) | 5927 | 158 | | |
| Target Length (cm) | | | 10 | |
| Target density [g/cm^3] | | | 0.1613 – 0.1617 | 0.0015 |
| Number of Kaon | | | 5.83×10^{10} | |
| Survival ratio of K^- | | | 0.281 | 0.0003 |
| DAQ live ratio | | | 0.768 | 0.0021 |
| Trigger efficiency | | | | |
| $K \otimes CDH1$ | | | 0.9527 | 0.0004 |
| Neutral | | | 0.9992 | 6.7×10^{-6} |
| Efficiency of the CDC | 0.977 | 0.04 | | |
| Acceptance of the NC (msr) | 21.5 | 0.2 | | |
| Efficeincy Of the NC | 0.291 | 0.015 | | |
| Intrinsic the NC | | | 0.317 | 0.016 |
| Over veto of the CVC/BVC | | | 0.081 | 0.007 |

Figure 1.45: This figure shows $d(K^-, n\pi^+\pi^-)''X''$ spectrum. Red line indicates fittig gaussian and gray hatched region indicates rejected region for $d(K^-, n\pi^+\pi^-)''n''$ events.

adopt 2σ selection in $d(K^-, n\pi^+\pi^-)''n''$ window to avoid the contamination. The $d(K^-, n\pi^+\pi^-)''n''$ peak was clearly seen, so we successfully identified $K^-d \rightarrow n\pi^+\pi^-n$ final state. The n detected by the NC is called as $n_{detected}$ and the other n is called as $n_{missing}$.

In $K^-d \rightarrow n_{detected}\pi^+\pi^-n_{missing}$ events, three type reactions were expected that shows below.

1. $K^-d \rightarrow K^0nn$
2. $K^-d \rightarrow \Sigma^\pm\pi^\mp n_{missing}$
3. $K^-d \rightarrow \Sigma^\pm\pi^\mp n_{detected}$

In reaction.1, the K^0 can be reconstructed from the π^\pm . In reaction.2, the neutron decayed from Σ^\pm is detected. So, Σ^\pm can be reconstructed from detected neutron and π^\pm . These 2 reactions can be identified from detected particles which was indicated in Fig1.46. Remained events should be reaction.3. In this reaction, K^- kicks neutron to forward and strangeness carried to backward and decay to $\pi^\mp\Sigma^\pm$. Left figure of Fig.1.47 shows missing mass of the $d(K^-, n)$ whose final state is identified the $K^-d \rightarrow n\pi^+\pi^-n$. K^0 and forward-going Σ^\pm tagged spectra was also shown in same figure.

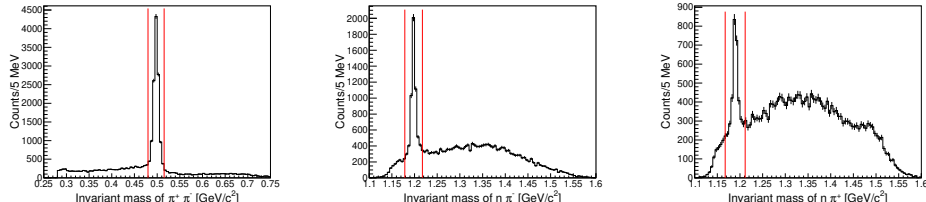


Figure 1.46: These figures show invariant masses of $\pi^+\pi^-$, $n\pi^-$ and $n\pi^+$ in $K^-d \rightarrow n\pi^+\pi^-n$ final state identified events, respectively. Red lines indicate select region for K^0 , $\Sigma_{forward}^-$ and $\Sigma_{backward}^+$, respectively.

1.4.13 template fitting of $d(K^-, n\pi^+\pi^-)''n''$ final state

K^0 tagged spectrum is seems to quasi-elastic scattering which will be arised from the $\bar{K}N$ threshold due to fermi motion. Strangeness was taken forward in $\Sigma_{forward}$ tagged events, so these are naturally expected to 1-step reaction. K^- -proton reactions have been studied about various final states and widely energy region[42], ofcouse $K^-p \rightarrow K^0n$ and $K^-p \rightarrow \pi^\mp\Sigma^\pm$ with $1GeV/c$ K^- have been studied[43]. Fermi motion in deuteron also have been studied from both theoretical and experimental side. So, we can simulate these quasi-elastic reactions. Angular distribution of K^- one nucleon reactions

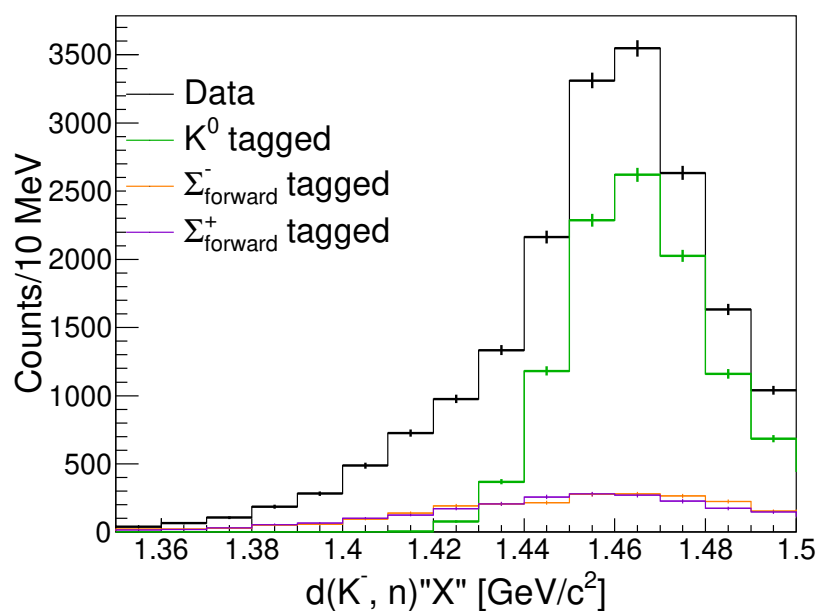


Figure 1.47: This figure shows the missing mass of $d(K^-, n)$ identified $d(K^-, n\pi^+\pi^-)''n''$ final state. Color plots show K^- and Σ_{forward} identified by invariant mass of detected particles. K^0 contamination is remained in quasi-elastic region. Σ_{forward} contaminations are negligibly small.

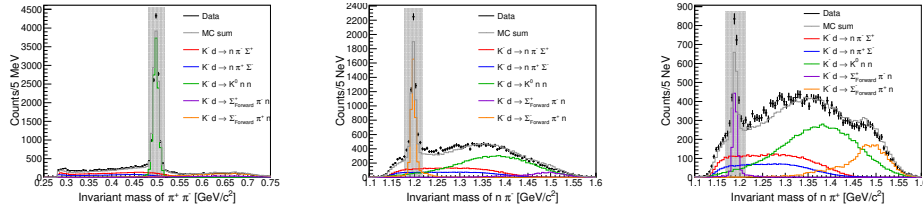


Figure 1.48: These figures shows invariant masses of $\pi^+\pi^-$, $n\pi^-$ and $n\pi^+$ with fitting result of 5 reactions.

were simulated previous experimental data and the other nucleon was regarded as spectator whose momentum was distributed fermi motion which was simulated previous experimental of $e(d, pn)$ reaction[46].

$d(K^-, n)\pi^\mp\Sigma^\pm$ reaction is regarded as 2-step reaction which is no data. In $d(K^-, n)\pi^\mp\Sigma^\pm$, detected neutron acceptance was restricted for super-forward angle so simulation data was produced using neutron angle within 8degree. Because momentum transfer around the $\bar{K}N$ threshold is small, the $\bar{K}N \rightarrow \pi^\mp\Sigma^\pm$ scattering is expected to S-wave. We adopt isotropic angular distribution in $\pi^\mp\Sigma^\pm$ decay. We adopt flat mass distribution of $\pi^\mp\Sigma^\pm$ from the $\bar{K}N$ threshold to $1.8 \text{ GeV}/c^2$ due to small phase space around the $\bar{K}N$ threshod.

We made 5 type template data using Geant4 which is Monte Carlo simulation toolkit for particle and nuclear physics[39] as follow.

$$K^-d \rightarrow nK^0 n_{spectator} \text{ (1-step reaction)} \quad (1.9)$$

$$K^-d \rightarrow \pi^-\Sigma^+ n_{spectator} \text{ (1-step reaction)} \quad (1.10)$$

$$K^-d \rightarrow \pi^+\Sigma^- n_{spectator} \text{ (1-step reaction)} \quad (1.11)$$

$$K^-d \rightarrow \pi^-\Sigma^+ n_{forward} \quad (1.12)$$

$$K^-d \rightarrow \pi^+\Sigma^- n_{forward} \quad (1.13)$$

The detail of the Monte Carlo using Geant4 was described in Set??.

These reactions was decomposed by so-called template fitting[44]. In this fitting, scaling factors are free parameters which was adjusted to reproduce the data spectrum and the criteria of goodness was adopted poisson/canonical distribution, so the template fitting considered statistics of the data spectrum and expected spectra.

There are two type fittings for the decomposition. One is invariant mass fitting of $\pi^+\pi^-$ and $n\pi^\pm$ for K^0 and $\Sigma_{forward}^\pm$ production. K^0 and $\Sigma_{forward}^\pm$ peaks could be reconstructed from invariant masses of $\pi^+\pi^-$ and $n\pi^\pm$, respectively. The other is $d(K^-, n\pi^\mp)X$ fitting for decomposition of the $\pi^\mp\Sigma^\pm$ modes. The $\pi^-\Sigma^+$ mode make $d(K^-, n\pi^-)\Sigma^+$ peak and widely distributes in $d(K^-, n\pi^-)X$ spectrum. Opposite charge is same as.

The reactions(1.9-1.11) can be simulated using angular distribution and fermi motion of the spectator that was well studied, so these reactions use

same template around whole events. On the other hand, there are no data about the branching ratio of the $d(K^-, n)\pi^\mp\Sigma^\pm$ modes that should be depend on the $\pi^\mp\Sigma^\pm$ mass. We should decompose each $d(K^-, n)\pi^\mp\Sigma^\pm$ modes each $\pi^\mp\Sigma^\pm$ mass from the data. For the resion, the fitting of the $d(K^-, n\pi^\mp)\Sigma^\pm$ was performed bin-by-bin of the $d(K^-, n)X$. Since the purpose of this analysis is determantion of the ratio of the $\pi^\mp\Sigma^\pm$ modes, We adopted this fitting to events rejected K^0 and $\Sigma_{forward}^\pm$.

We iteratively performed these fittings and the other parameters were fixed. Thus, the $d(K^-, n)\pi^\mp\Sigma^\pm$ spectra were fixed in the invariant mass fitting. On the other hand, spectra simulated 1-step K^0 and $\Sigma_{forward}^\pm$ reactions were fixed in the $d(K^-, n\pi^\mp)X$ fitting.

We estimated each reactions' template spectra of $\pi^+\pi^-$ and $n\pi^\pm$ invariant masses as Fig1.48. Although the $d(K^-, n\pi^\mp)X$ fitting was adopted to events rejected K^0 and $\Sigma_{forward}^\pm$, contamination from these reactions was estimated from invariant mass fittings which was considered in the $d(K^-, n\pi^\pm)X$ fitting. The $d(K^-, n\pi^\mp)X$ spectra were reproduced as shown in Fig1.49. The $d(K^-, n\pi^\mp)X$ fitting was performed each bins of $d(K^-, n)\pi^\mp\Sigma^\pm$ whose likelihood was shown in same figure. Reproduced spectra in each bin were also shown in Fig1.51

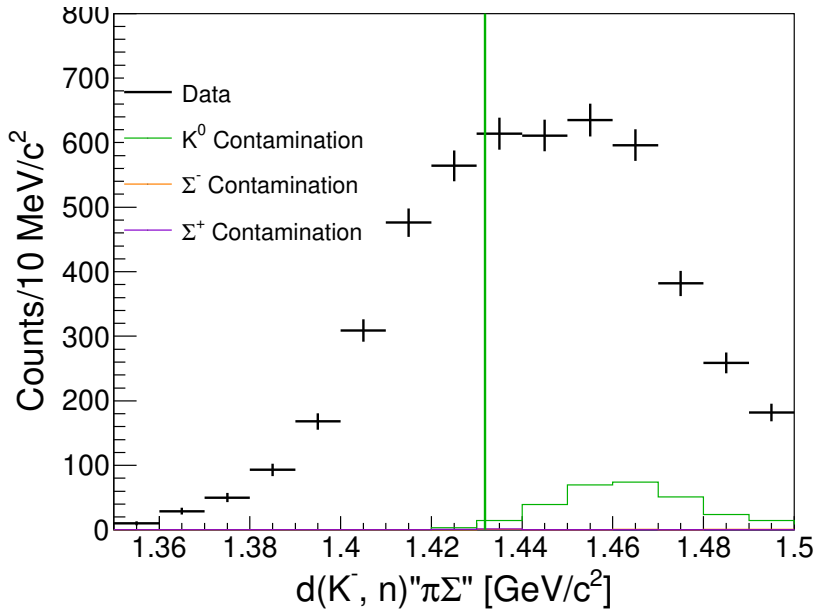


Figure 1.49: The figure shows $d(K^-, n)\pi^\pm\Sigma^\mp$ which was identified to reject events identified K^0 and $\Sigma_{forward}$ from detected particles. Color plots indicate contamination estimated by the template fitting of invariant masses.

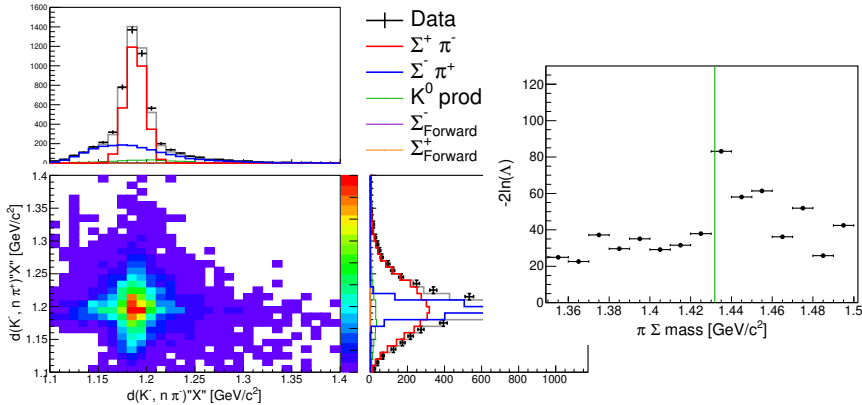


Figure 1.50: This figure indicates summed up fitting result and log-likelihood value of each bins.

1.4.14 The cross section of K^0

K^0 identified events is the most strongly candidate to search 1-step reaction of $\bar{K}N$, although the reaction can not measured below the $\bar{K}N$ threshold. Because $d(K^-, n)\pi^\mp\Sigma^\pm$ reactions is difficulty to reject, each background can be estimated like Fig1.48. Fig[?] indicates $d(K^-, n)nK^0$ missing spectrum with estimated backgrounds by template fitting Sec.1.4.13 (left figure) and K^0 selection gate which is same right figure of Fig1.48 (right figure) without spectra estimated by the Monte Carlo. In this reaction, $d(K^-, n)$ was rised from the $\bar{K}N$ threshold due to fermi motion of spectator. The acceptance of this reaction was defined by the K^0 kinematics which was detected by the CDS and reconstructed. So, we estimated the acceptance as function of K^0 's $\cos\theta$ and momentum. We simulate $K^-d \rightarrow K^0nn$ event with flat mass distribution of nK^0 for statistics near the threshold. Another neutron was scattered forward angle and this neutron was detected by the NC. The acceptance was estimated by this simulation as Fig1.54. $d(K^-, n)K^0n$ spectrum was corrected the acceptance event by event using this 2 dimensional acceptance. We obtain acceptance corrected spectra as shown in Fig??. We simultaneously obtain background which was estimated by the Monte Calro simulation to adopt same procedure to background process. Fig1.55 represents scatter plot of angle and momentum of K^0 using data and background process. Data distribution concentrate to backward and 0.2GeV region which had low acceptance. On the other hand, background process widely distribute. By this reson, signal was enhanced by the acceptance correction. We obtain the cross section of $d(K^-, n)nK^0$ to substrat background and adopt conversion factor of summized Table1.2 which was shown in Fig1.57

These distribution of data was shown in Fig1.55.

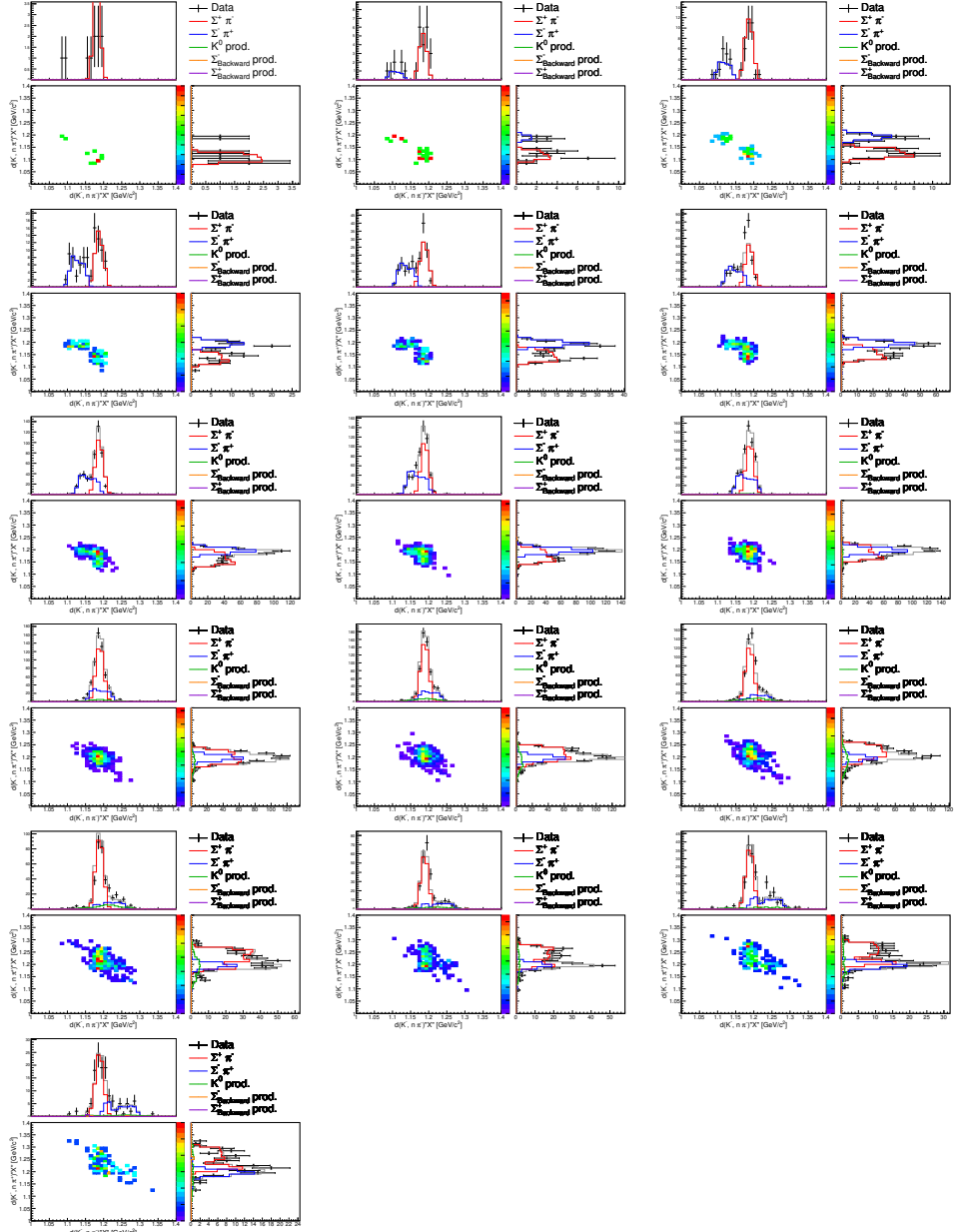


Figure 1.51: These figures indicate fitting results of each bins of $d(K^-, n)\pi^\pm\Sigma^\pm$ whose bin width is $10\text{MeV}/c^2$. Upper left figure shows about $1.35 \sim 1.36\text{GeV}/c^2$ bin and the figure just to the right shows about $1.36 \sim 1.37\text{GeV}/c^2$ bin. So, lower left figure shows about $1.49 \sim 1.50\text{GeV}/c^2$ bin.

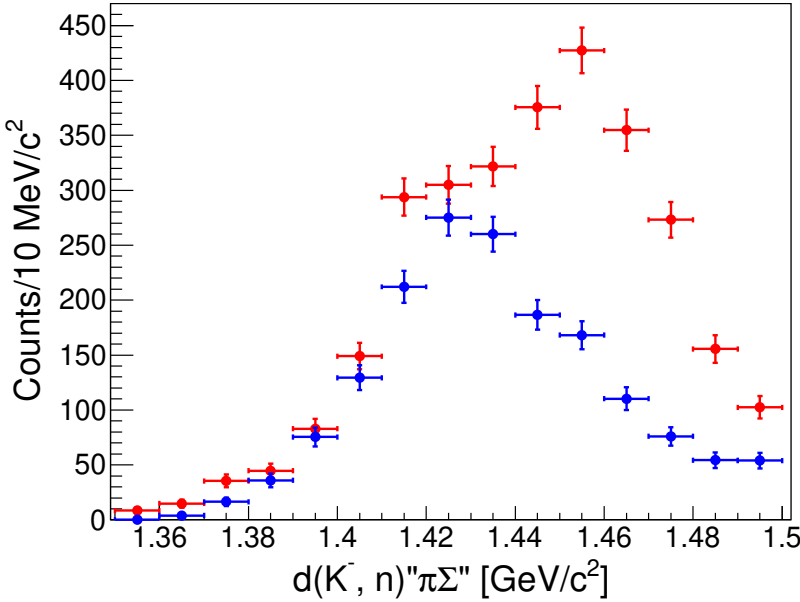


Figure 1.52: This figure indicates decomposed number of $d(K^-, n)''\pi^-\Sigma^+$ and $d(K^-, n)''\pi^+\Sigma^-$ modes. In this figure, K^0 2-step reaction effect is including which described Sec.1.59.

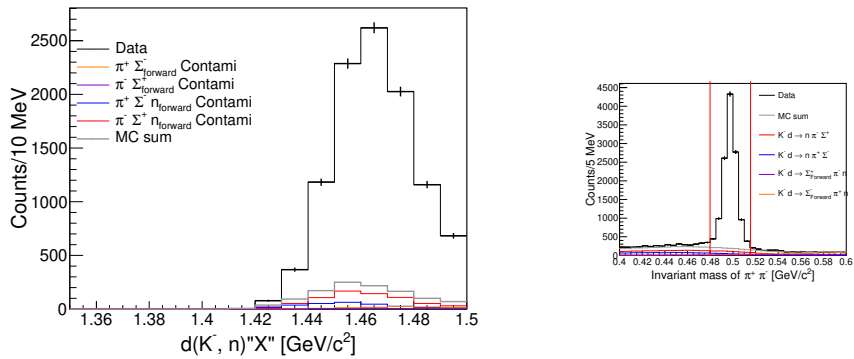


Figure 1.53: Right figure shows K^0 selection region and estimated background events which is zoom up of left figure of Fig1.48. Red lines indicate selection region. left figure shows $d(K^-, n)''nK^0''$ spectra with esmated backgrounds by MC template.

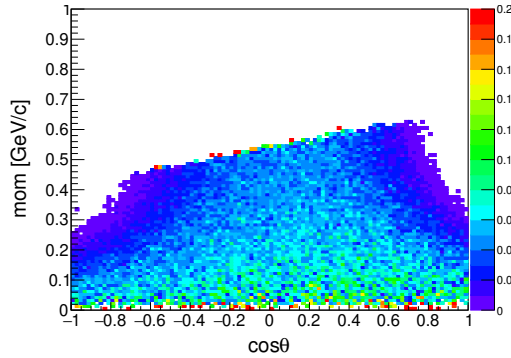


Figure 1.54: This figure shows the acceptance of the $K^-d \rightarrow K^0 nn$ reaction which was estimated by the Monte Carlo simulation.

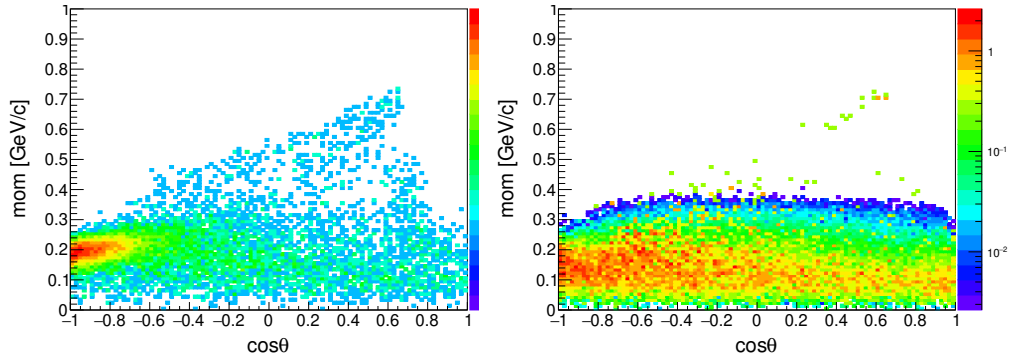


Figure 1.55: These figure shows about K^0 emit angle and momentum in the experimental frame. Left figure shows about data and right figure shows background estimated by the Monte Carlo.

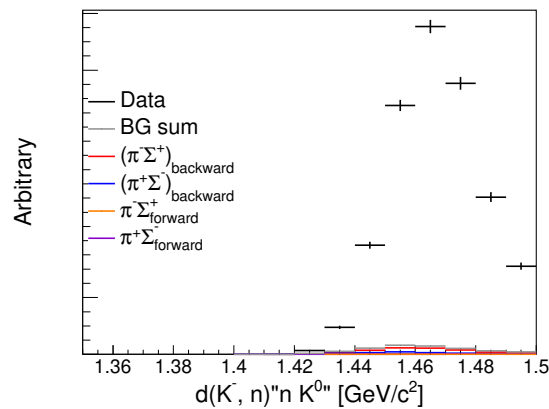


Figure 1.56: This figure shows acceptance corrected spectrum of the $d(K^-, n)n K^0 nn$. Black line indicates data and color plots indicate the background reproduced by the Monte Carlo simulation.

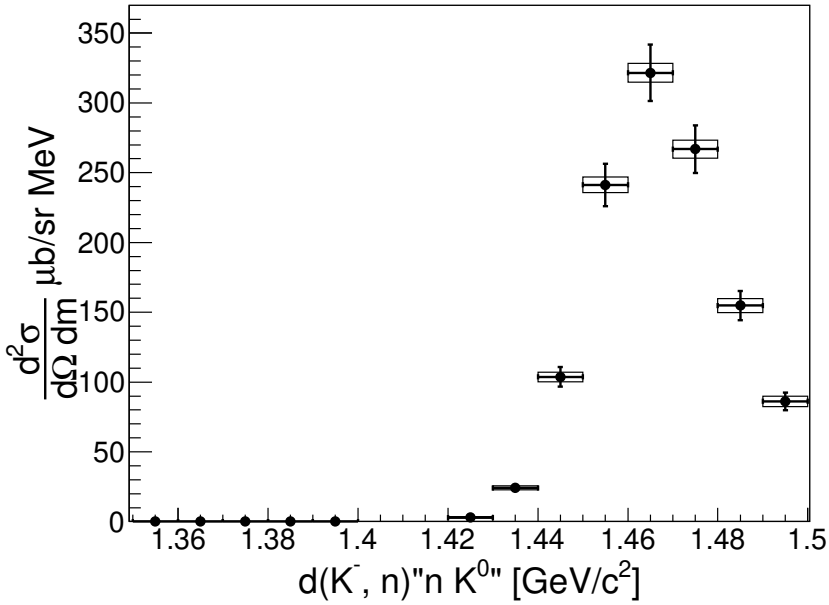


Figure 1.57: This figure shows the cross section of the $d(K^-, n)"n K^0"$. Box indicates statistical errors and error bar indicates errors convolved conversion factors which summarized at Table1.2

1.4.15 The cross section of the $d(K^-, n)"\pi^\mp\Sigma^\pm$

The Monte Carlo simulation of $d(K^-, n)"\pi^\mp\Sigma^\pm$ reaction was performed to decompose each modes. The simulation data was used to estimate the acceptance as function of $d(K^-, n)"\pi^\mp\Sigma^\pm"$ to adopt same analysis procedure, so this acceptance includes $d(K^-, n\pi^+\pi^-)"n"$ selection efficiency , rejection ratio of $\Sigma_{forward}^\pm$ and K^0 and so on. Fig1.58 shows these acceptances. Spectra of the $d(K^-, n)"\pi^\mp\Sigma^\pm"$ was converted to the cross section these acceptances and conversion factor which was summarized at Table1.2. Obtained cross sections are represented at Fig1.59. Inner box indicates statistical error of the $d(K^-, n)"\pi^\mp\Sigma^\pm"$ events, outer box indicates errors convolved fitting error and error bars indicates error including all error which is statistical error, fitting error and conversion factor error.

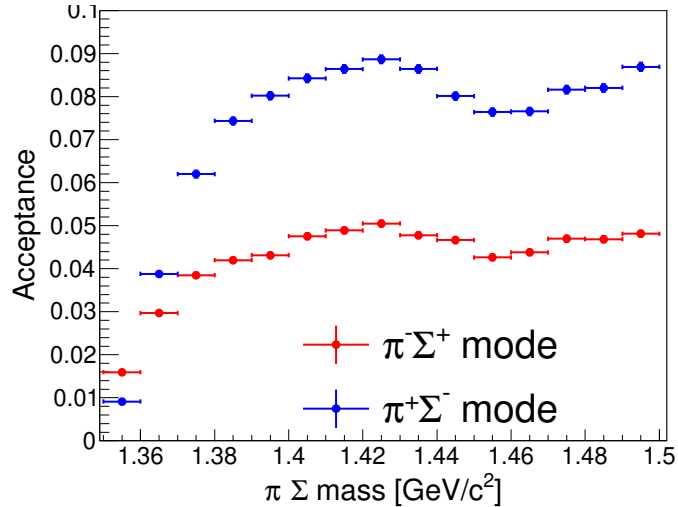


Figure 1.58: This figure shows the acceptance of $d(K^-, n)\pi^\mp\Sigma^\pm$ modes.

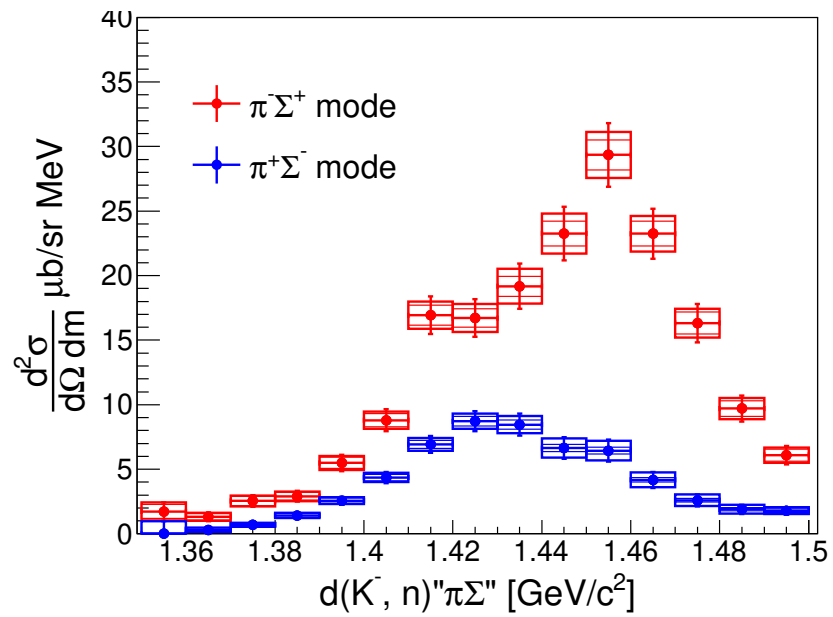


Figure 1.59: This figure shows cross sections os $d(K^-, n)\pi^\mp\Sigma^\pm$ which convolve K^0 2step effect discribed at Sec.

Bibliography

- [1] M. H. Alston, L. W. Alvarez, P. Eberhard and M. L. Good, Phys. Rev. Lett. 6, 698 (1961).
- [2] R. D. Tripp, R. O. Bangerter, A. Barbaro-Galtieri and T. S. Mast, Phys. Rev. Lett. 21, 1721 (1968).
- [3] R. J. Hemingway, Nucl Phys B **253**, 742 (1985).
- [4] R. H. Dalitz and A. Deloff, J. Phys. G17, 281 (1991).
- [5] A. D. Martin, Nucl. Phys. B **179**, 33 (1981).
- [6] M. Tanabashi et al., Phys. Rev. D **98**, 030001 (2018).
- [7] M. Iwasaki et el., Phys. Rev. Lett. **78**, 3067 (1997).
- [8] G. Beer et al., Phys. Rev. Lett. **94**, 212302 (2005).
- [9] M. Bazzi et el., Phys. Lett. B **704**, 113 (2011).
- [10] Y. Nagomi, Physc. lett. **7**, 288 (1963).
- [11] Y. Akaishi and T. Yamazaki, Phys. Rev. C **65**, 044005 (2002).
- [12] M. Agnello fot the FINUDA Collaboration, Phys. REv. Letts. **94**, 212303 (2005).
- [13] R. Del Grande et el., Eur. Phys. J. C. **79**, 190 (2019).
- [14] T. Yamazaki et el., Phys. Rev. Lett. **104**, 132502 (2010).
- [15] G. Agakishiev et el., Phys. Lett. B **742**, 242 (2015).
- [16] A. O. Tokiyasu fot the LEPS Collaboration, Phys. Lett. B **728**, 616 (2013).
- [17] T. Yamazaki and Y. Akaishi, Phys Lett. B. **535**, 70 (2002).
- [18] Y. Ichikawa et el., Prog. Theor. Exp. Phys. 021D01 (2015).

- [19] T. Yamaga for the E15 Collaboration, Phys. Rev. B **789**, 620 (2019).
- [20] D. Jido et el., Nucl. Phys. A **725**, 181 (2003).
- [21] Jonathan M.M. Hall et el, Rhys. Rev. Lett. **114**, 132002 (2015).
- [22] T. Hyodo and D. Jido, Prog. Part. Nucl. Phys. **67**, 55 (2012).
- [23] M. Niiyama et el., Phys. Rev. C **78**, 035202 (2008).
- [24] K. Moria for the CLAS Collaboration, Phys. Rev. Lett. **112**, 082004 (2014).
- [25] G. Agakishiev for the HADES Collaboration, Phys. Rev C **87**, 025201 (2013).
- [26] L.Fabbietti et el., Nucl. Phys. A **914**, 60 (2013).
- [27] O. Braun et el., Nucl. Phys. B **129**, 1 (1977).
- [28] D. Jido, E. Oset and T. Sekihara, Eur. Phys. J. A **42**, 257 (2009).
- [29] K. Miyagawa and J. Haidenbauer, Phys. Rev. C **85**, 065201 (2012).
- [30] S. Ohnishi et el, Phys. Rev. C **93**, 025207 (2016).
- [31] H. Kamano et el., Phys. Rev. C **90**, 065202 (2014). Phys. Rev. C**92**, 025205 (2015). Phys. Rev. C**95**, 044903(E) (2015).
- [32] H. Kamano et el., Phys. Rev. C**94**, 065205 (2016).
- [33] K. Agari et el, Prog. Theor. Exp. Phys., 02B009 (2012)
- [34] K. Agari et el, Prog. Theor. Exp. Phys., 02B011 (2012)
- [35] TRANSPORT <http://linac96.web.cern.ch/Linac96/Proceedings/Thursday/THP72/Paper.pdf>
- [36] T. K. Ohska et al., Nuclear Science, IEEE Transactions on **33**, 98 (1986).
- [37] M. Shiozawa and et el., A new TKO system manager board for a dead-time-free data acquisition system, in 1994 IEEE Nuclear Science Symposium-NSS'94, pages 632635, (1994)
- [38] M. Iio et al., Nucl. Instrum. Methods Phys. Res., Sect. **A** 687, 1 (2012).
- [39] S. Agostinelli et al., Nucl. Instrum. Methods Phys. Res., Sect. **A** 506, 250 (2003)
 J. Allison et al., IEEE Transactions on Phys. Sci. **53**, 207 (2006)
 J. Allison et al., Nucl. Instrum. Methods Phys. Res., Sect. **A** 835, 186 (2016)

- [40] K. Fuji, https://www-jlc.kek.jp/subg/offl/lib/docs/helix_manip/node3.html (1968).
- [41] <https://operafea.com/>
- [42] V. Flaminio et al., CERN-HARA-87-01, 121 (1983).
- [43] M.Jones et el, Nucl. Phys. B **90**, 349 (1975)
- [44] R. Barlow and C. Beeston, Comp. Phys. Comm. **77**, 219 (1993).
- [45] M. jones, R. Levi, Setti, D. Merrill and R. D. Tripp, Phys. Rev. B**90**, 349 (1975).
- [46] M. Bernheim and et. el., Nucl. Phys. A**365**, 349, (1981).
- [47] R. Machleidt, Phys. Rev. C**63**, 024001 (2001).
- [48] S. Agostinelli et al., Nuclear Instruments and Methods in Physics Research Section A: Accelerators, Spectrometers, Detectors and Associated Equipment **506**, 250 (2003).
J.Allison et el., Nuclear Instruments and Methods in Physics Research Section A: Accelerators, Spectrometers, Detectors and Associated Equipment **835**, 186 (2016).